DISCLAIMER

Pacific Northwest
NATIONAL LABORATORY

PNNL-33278

Selective Thermal Emission with Radiation and Adsorption in Annuli (STERADIAN): An Advanced Heat Exchanger Concept for Supercritical CO_2 Power Cycles

January 2022

B. P. McGrail
B. E. Bernacki
O. Ilic
J. L. Loring
C. C. Bonham
H. T. Schaef
D. J. Baker
J. J. Jenks
N. Lahiri

U.S. DEPARTMENT OF ENERGY

Prepared for the U.S. Department of Energy
under Contract DE-AC05-76RL01830

DISCLAIMER

PACIFIC NORTHWEST NATIONAL LABORATORY
operated by
BATTELLE
for the
UNITED STATES DEPARTMENT OF ENERGY
under Contract DE-AC05-76RL01830

Printed in the United States of America

Available to DOE and DOE contractors from the Office of Scientific and Technical Information,
P.O. Box 62, Oak Ridge, TN 37831-0062
www.osti.gov
ph: (865) 576-8401
fax: (865) 576-5728
email: reports@osti.gov

Available to the public from the National Technical Information Service
5301 Shawnee Rd., Alexandria, VA 22312
ph: (800) 553-NTIS (6847)
or (703) 605-6000
email: info@ntis.gov
Online ordering: http://www.ntis.gov

PNNL-33278

Selective Thermal Emission with Radiation and Adsorption in Annuli (STERADIAN): An Advanced Heat Exchanger Concept for Supercritical CO_2 Power Cycles

January 2022

B. P. McGrail
B. E. Bernacki
O. Ilic[1]
J. L. Loring
C. C. Bonham
H. T. Schaef
D. J. Baker[2]
J. J. Jenks
N. Lahiri

Prepared for
the U.S. Department of Energy
under Contract DE-AC05-76RL01830

Pacific Northwest National Laboratory
Richland, Washington 99354

[1]University of Minnesota
Minneapolis, Minnesota 55455

[2]Washington Nanofabrication Facility
Seattle, WA 98105

Abstract

One of the key limitations affecting ability to achieve the efficiency and cost saving advantages of a supercritical CO_2 ($scCO_2$) power cycle resides with the primary heat exchanger where costs can exceed 50% of the plant capital budget depending on design. This project established the foundational groundwork for a new type of heat exchanger optimized to take advantage of radiative heat transfer to $scCO_2$. Selective thermal emission coatings were designed and tested that radiated more light tuned to the 4.2 μm infrared absorption band of CO_2. Coating design utilized principles of nanophotonic bandgap theory to design a selective emitter that has: 1) low emissivity in the visible band, 2) near 100% effective emissivity in the mid-IR wavelength between 4 and 4.5 μm wavelength, and 3) strong suppression of far-IR light emission that will maximize radiative heat transfer efficiency to $scCO_2$. Computational fluid dynamics simulations show that an advanced heat exchanger implementing this selective thermal emitter coating is 25 to as much as 40% smaller than conventional heat exchanger designs.

Acknowledgments

The material in this report is based upon work supported by the U.S. Department of Energy's Office of Energy Efficiency and Renewable Energy (EERE) under the Solar Energy Technologies Office (SETO) Award Number 35935. The authors also gratefully acknowledge the sample fabrication assistance provided by the Washington Nanofabrication Facility, a shared user facility that provides open access to leading-edge micro and nanofabrication processing equipment.

Contents

Figures

Tables

1.0 Introduction

The supercritical carbon dioxide ($scCO_2$) Brayton cycle is of particular interest to SETO because it is a viable candidate to satisfy cost and efficiency targets for new power generation in 2025 and beyond. This is primarily due to potential to achieve high conversion efficiency (>40%), dry cooling compatibility, and small size (influencing capital and O&M costs). One of the limitations affecting ability to achieve the efficiency and cost saving advantages of a $scCO_2$ power cycle resides with the primary heat exchanger shown in **Figure 1**. Because $scCO_2$ has a much lower convective heat transfer coefficient compared with water (5 to 20X lower), a much larger and concomitant higher cost heat exchanger is required to support an equivalent power output. This problem becomes progressively more severe with designs pushing temperatures of the $scCO_2$ above 900°C where heat exchanger costs can exceed 50% of the plant capital cost depending on design [1]. Approaches to reduce these impacts have so far focused on well-known methods of heat transfer enhancement, such as use of microchannel or microtube heat exchanger designs. There has also been recent attention on use of cermets with enhanced high-temperature failure strength, thermal conductivity, and corrosion resistance that could provide an attractive combination of properties for a robust heat exchanger.

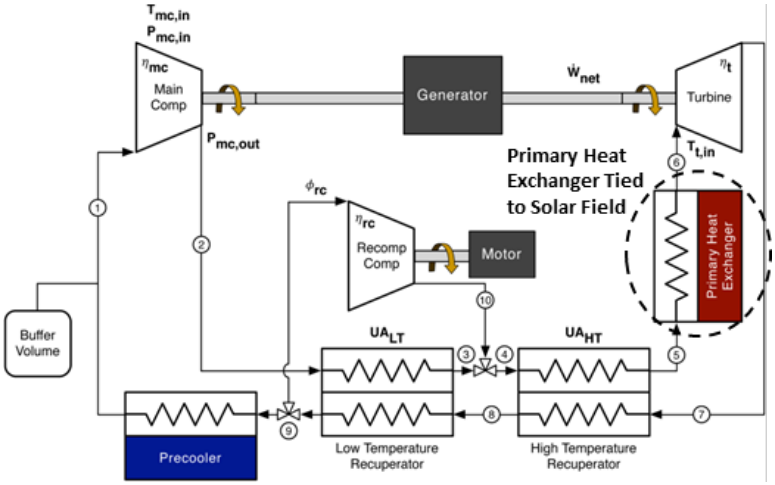

Figure 1. Schematic of basic $scCO_2$ power system

A factor that has been largely ignored in heat exchanger designs for $scCO_2$ is the role that radiative heat transfer could potentially play in overcoming heat transfer limitations. Many heat transfer studies involving $scCO_2$ treat it as a "non-participating" medium where radiation is assumed to have negligible influence on the overall heat transfer [2-6]. Radiation from a *normal* (more on this later) surface approximately follows the Stefan-Boltzmann law as illustrated in Figure 2 where the total radiance from the surface is proportional to the fourth power of its absolute temperature. Radiative heat transfer thus becomes an increasingly important consideration as operating temperatures climb above 700°C. A numerical modeling study [7] showed significant impacts of including radiative heat transfer on CO_2 temperature rise in a 2 cm diameter pipe with a constant wall temperature of 1100K under certain conditions. However, no attempt was made to simulate a more optimized design for the heat exchanger to take advantage of the radiative heat transfer. Khivsara, Srinivasan, and Dutta [8] showed that under a constant heat flux condition, there is a range

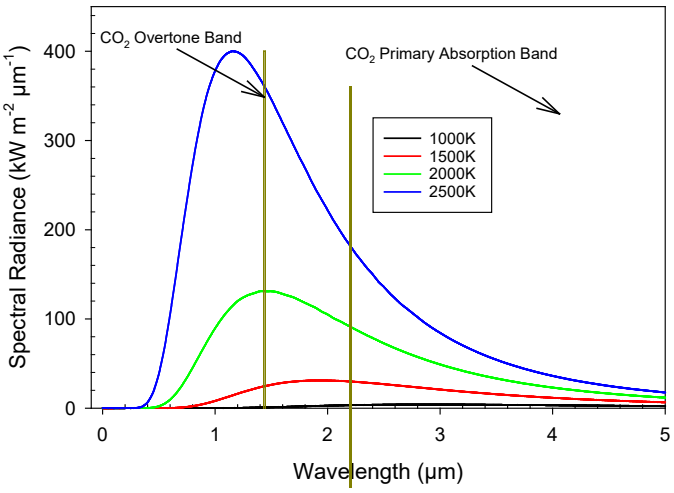

Figure 2. Comparison of radiated light from a blackbody source versus absorption bands of $scCO_2$

of flow rates over which the radiative heat transfer contribution is significant, reaching about 25% of the total heat transfer when high emissivity values were assumed for the heat exchanger wall surface. Still, the broadband radiated light from a normal hot surface has <5% of the radiated power where it can be effectively absorbed by CO_2, as illustrated in Figure 2.

The core objective of this project is to lay the groundwork for a new type of heat exchanger optimized to take advantage of radiative heat transfer to $scCO_2$. To do that, we designed selective thermal emission coatings that radiate light tuned to the 4.2 μm infrared absorption band of CO_2. Selective thermal emitters have received extensive attention recently to help improve efficiency of thermophotovoltaic (TPV) direct power conversion systems. In TPV systems, the role of the selective emitter is to tune the emission spectrum for the effective bandgap region of the PV material(s) used in the device, typically on the order of 0.7 eV or 1.7 μm for low bandgap semiconductors. The R&D challenge in this project is to develop a high-temperature stable selective emitter such as has been demonstrated with plasmonic W/HfO_2 gratings [9] combined with an emission spectrum tuned for the correct mid-IR 4.2 μm band as has been demonstrated at 300°C for a Ag/SiO_2 grating [10]. **Figure 3** shows a configuration for a $scCO_2$ heat exchanger implementing this Selective Thermal Emission with Radiation and Adsorption in Annuli (STERADIAN) concept [11].

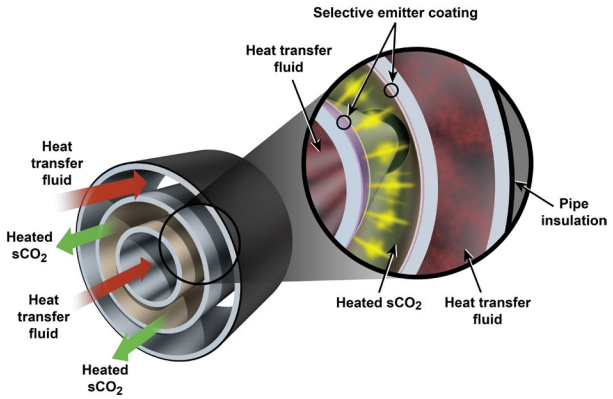

Figure 3. Schematic of application of selective thermal emitter in a $scCO_2$ heat exchanger

In controlling the light spectrum from a selective thermal emitter for a $scCO_2$ heat exchanger, the desired properties include: 1) low emissivity in the visible band, 2) near 100% effective emissivity in the mid-IR wavelength between 4 and 4.5 μm wavelength, and 3) strong suppression of far-IR light emission. The use of selective thermal emitters for TPV applications is known, but the target emitter temperatures in this proposal (up to 700°C) require consideration of metamaterial stability at high temperatures as well as effective approaches to thermal-radiation recycling. We utilized principles of nanophotonic bandgap theory to design the selective metamaterial thermal emitter. Key design objectives and outcomes are:

- Identify suitable materials for the thermal emitter. Key consideration for the metamaterial emitter is temperature stability so we investigated refractory materials including tantalum, tungsten, and titanium nitride. For far-IR selective filtration, we focused on dielectric materials of varying refractive index such as Al_2O_3, Ta_2O_5, TiO_2, and ZrO_2.
- Determine optimal photonic crystal or super-lattice thermal emitter design. The primary consideration was maximization of emissivity at the desired mid-IR wavelengths. We set out to achieve this by matching the radiative and the absorptive quality factors Q_{rad} and Q_{abs} of the photonic crystal resonances. Optimized structures were then be found using Rigorous Coupled Wave Analysis or Finite Difference Time Domain to probe the relevant dimensions, thicknesses, and aspect ratios of the features. These modeling tools were supplemented as needed with advanced numerical optimization tools [12] for photonic filter theory. IR spectroscopy measurements were then performed to collect emission spectra of synthesized selective emitters at temperatures up to 1000°C.

2.0 Selective Emitter Design

Design of selective emitter coatings (SECs) was performed around two distinct types of structural motifs: 1) Thin film, and 2) Photonic crystal. Thin-film SECs have advantages in terms of manufacturing simplicity and mature scalable techniques such as magnetron sputtering, solution plasma spray, atomic layer deposition, and several other methods that can be adapted to coating large heat exchanger surfaces. Thin film deposition is also readily conformal to complex and curved surfaces that may be required in some heat exchanger designs. The main drawbacks to thin-film SECs involve the multiple layers (interfaces) that will have mismatches in coefficient of thermal expansion that could lead to delamination with thermal cycling and polarization and emissivity angular dependencies that may diminish overall effectiveness of the coating's radiated power in the targeted mid-IR band. Photonic crystal motifs consist of a periodic array of sub-wavelength structures such as pillars, crosses, or cavities. The periodic structure gives rise to band gaps caused by destructive interference of multiple reflections of light propagating in the crystal at the interfaces of high- and low-dielectric constant regions [13]. The main advantages of the PhC motif are very narrowband performance and potentially superior thermal ruggedness due to far fewer interfaces with dissimilar materials as compared to thin-film SECs. The main disadvantages involve barriers to manufacturing scalability due to need for sophisticated lithography techniques to create the periodic structures and consequent higher manufacturing costs.

The following sections detail the design efforts completed on both SEC structural motifs.

2.1 Thin-Film Motif

2.1.1 Distributed Bragg Reflector (DBR)

A multilayer film approach was examined that exploits the use of a distributed Bragg reflector (DBR) structure, based on the approach described by Yang et al. [14]. This approach is advantageous as the authors describe a structure in which the DBR is the input plane, with the structure arrayed on top of a thick metal substrate separated by a dielectric spacer layer, as is envisioned for the proposed heat exchanger. In this design, only the design of the DBR stack influences the wavelength performance as opposed to metal-side designs (essentially Fabry-Pérot designs) in which a precisely controlled thin metal thickness is part of the design. A graphic from the Yang paper showing the two approaches is shown below in Figure 4, along with our modified design tuned for the 4.2 μm desired emittance peak for several candidate metals.

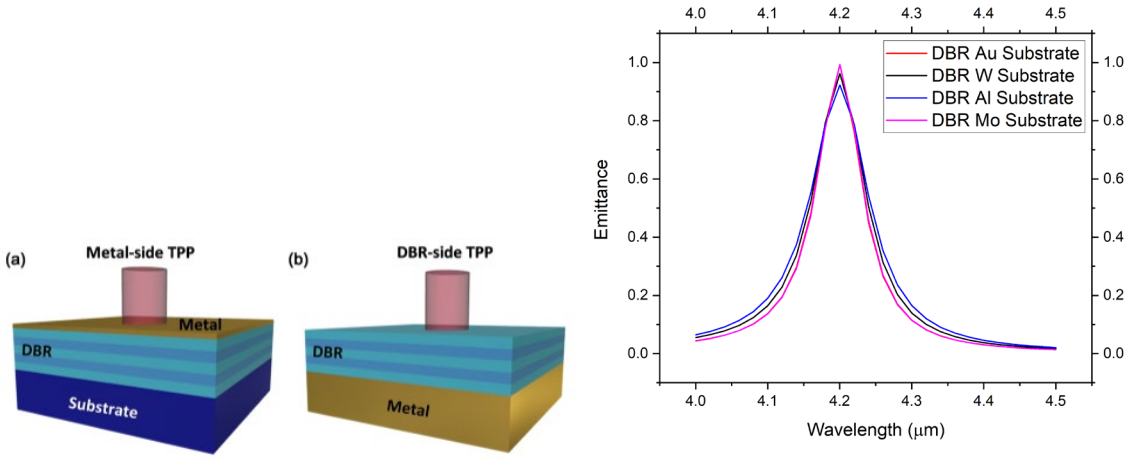

Figure 4. Two approaches to fabricating a DBR enhanced emittance structure are shown (above left: metal-side entry and DBR-side entry. The DBR-side approach is preferred for this application. Calculations for various metal thick films for the DBR-side design (above right) for illumination at normal incidence.

The major benefit for the DBR-side reflector is that the structure can be integrated with a metallic heat exchanger design and only the number of DBR pairs consisting of Si/SiO_2 layers determines the reflectance (emittance = 1 - reflectance) and not the metal thickness in the case of the metal-side approach. The metal layer must just be "thick enough" to serve as a reflector in the wavelength range of interest. In Figure 4, the design shown consisted of two DBR pairs of Si/SiO_2 with thicknesses of 392.2/765.1 nm, respectively with a 262.1 nm Si matching layer on substrates of Au, Al, W, and Mo. Modeling was accomplished with Essential Macleod, a thin film design, modeling and optimization software package based on the transfer matrix method (TMM). The TMM exploits the Fresnel equations and continuity of the E-field across layer boundaries. The solution is exact, but it can only be used on stratified media, such as the DBR or other thin film designs. The optical simulations of the DBR-side design show that the coating achieves a narrow emissivity band at our desired wavelength with a very high emissivity coefficient in this band.

A recent publication[15] proposed titanium nitride (TiN) based coatings for high-temperature selective emitter applications. Although two approaches using TiN were proposed, one exploiting Tamm plasmon polaritons (TPP) and a second using Metal-Insulator-Metal construction (MIM), modeling analysis revealed that the TPP approach was superior as the MIM approach required critical control of the metal-incident layer and displayed more harmonics. An illustration of the structure of the DBR-side approach is provided in Figure 5, which shows the 200 nm TiN layer and the single distributed Bragg reflector.

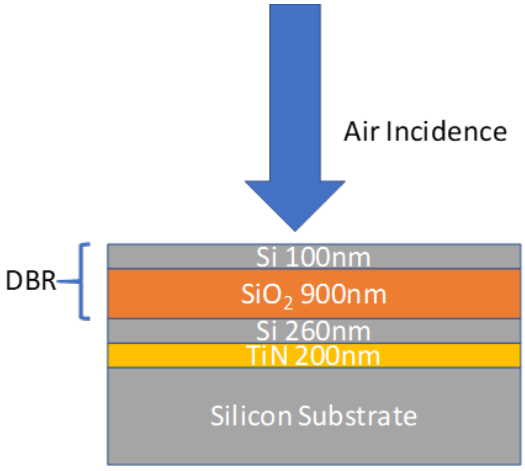

Figure 5. Design showing TPP approach using TiN and single distributed Bragg reflector.

When the design is optimized for enhanced emittance in the wavelength region required for $scCO_2$, shown in Figure 6a, the resulting emittance is nearly 0.95. Moreover, the design has a low sensitivity to fabrication errors. This

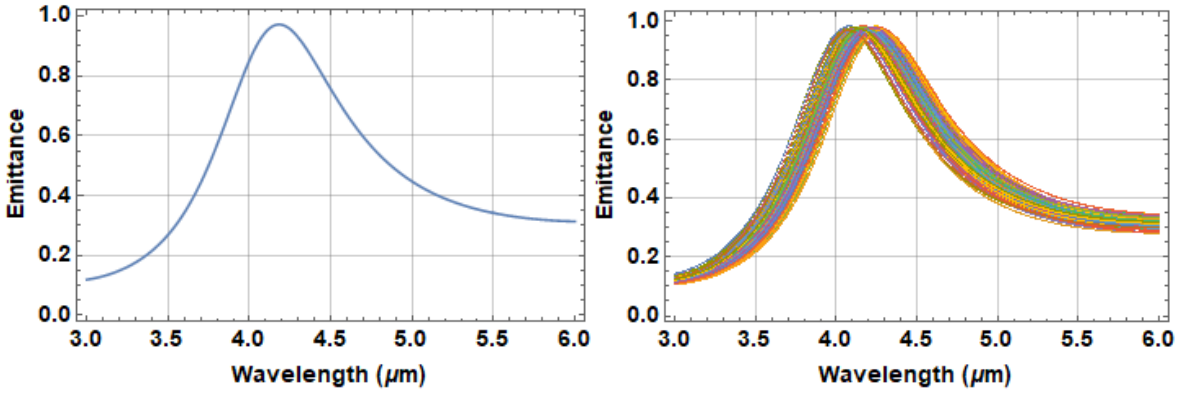

Figure 6. Emittance versus wavelength for the TiN-TPP approach (above left) showing excellent emittance in the desired wavelength region for $scCO_2$ heat transfer. Additionally, the design is insensitive to less stringent fabrication tolerances. In the above right plot, a Monte Carlo analysis over 100 trials was performed in which the film thickness could vary by several nanometers with little or no reduction in emittance performance and only small shift in the center wavelength of the response function.

is demonstrated through a sensitivity analysis regarding fabrication errors (Figure 6b). The Si and TiN layers were permitted 2 nm errors, and the SiO_2 layer a potential thickness error of 5 nm. After 100 trials, the performance has only slightly degraded, demonstrating the fabrication robustness of this design.

The distributed Bragg reflector (DBR) selective emitter coating shown in Figure 5 was further examined to determine if alternate stack materials could reduce potential issues with layer stability (mechanical/chemical) when operating for extended periods at high temperature. In the original design, the melting point of Si at 1,414°C might limit some applications. The Si layers were replaced by SiC (m.p. 2,730°C), while the SiO_2 layer was replaced with HfO_2 (m.p. 2,758°C). TiN, being a refractory ceramic, has a m.p. of 2,930°C. The revised stack composition is shown in Figure 7. Also included in this design is an IR-transparent capping layer designed to help protect the underlying thinner selective emitter coating. Yttria stabilized zirconia is one example material that would be suitable for the capping layer and is readily applied with EB-PVD or suspension plasma spray processes.

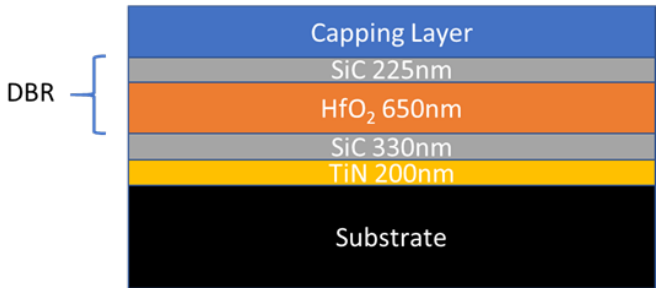

Figure 7. Revised DBR design with SiC substituted for Si, and HfO_2 replacing SiO_2

For comparison, the predicted emittance of both designs is plotted versus wavelength in **Figure 7**. Key finding from this analysis is that there is no emission performance penalty in substituting the higher m.p. materials for Si and SiO_2. In summary, the revised design substituting higher m.p. materials shows that additional materials selection options are available to alleviate stability issues with these multi-layer designs. Although Si and SiO_2 have lower coefficients of thermal expansion (CTE) than that of SiC and HfO_2, the CTE of SiC (8 to 11 x 10^{-6}/K) is better matched to the CTE for TiN (~9.4 x 10^{-6}/K) versus the CTE of Si (2.6 x 10^{-6}/K) so this revised design may be more resistant to delamination under thermal cycling.

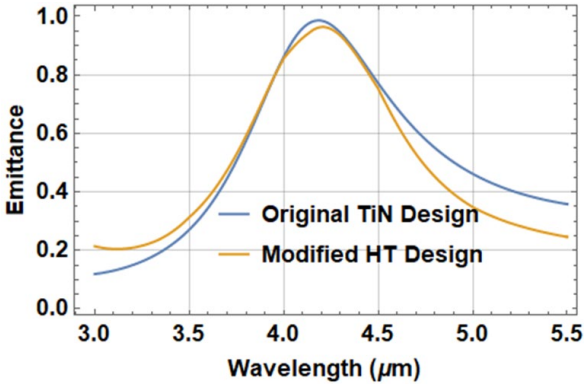

Figure 8. Plots of emittance versus wavelength are shown for the original DBR-TiN design that uses Si/SiO_2 for the DBR layers versus the high temperature (HT) version that substitutes SiC and HfO_2 for these materials. The performance is comparable for the two designs with the added advantage of better overall CTE match for the stack.

2.1.2 Coupled-Mode Systems

The team at UMN also explored alternative thin-film designs that maximize the total radiated power efficiency η. To maximize the emission of thermal radiation in the 4-4.5 μm range that is relevant, an optimization figure of merit η was derived to quantify the fraction of emission in the desired wavelength range relative to the total emission at all wavelengths, namely:

$$\eta = \frac{\int_{4\mu m}^{4.5\mu m} \epsilon_H(\lambda)\pi I_b(\lambda,T)\, d\lambda}{\int_0^{\infty} \epsilon_H(\lambda)\pi I_b(\lambda,T)\, d\lambda} \quad (1)$$

where ϵ_H is the hemispherical emittance and I_b is the blackbody spectral intensity.

The analysis was performed using UMN's efficient formulation of the transfer matrix method coupled to gradient-based optimization routines. Initial designs were informed by coupled-mode photonic theory of narrowband thermal emission. Conceptually shown in Figure 9a, the target arrangement consists of a core (metallic) background that couples to a thin-film resonant

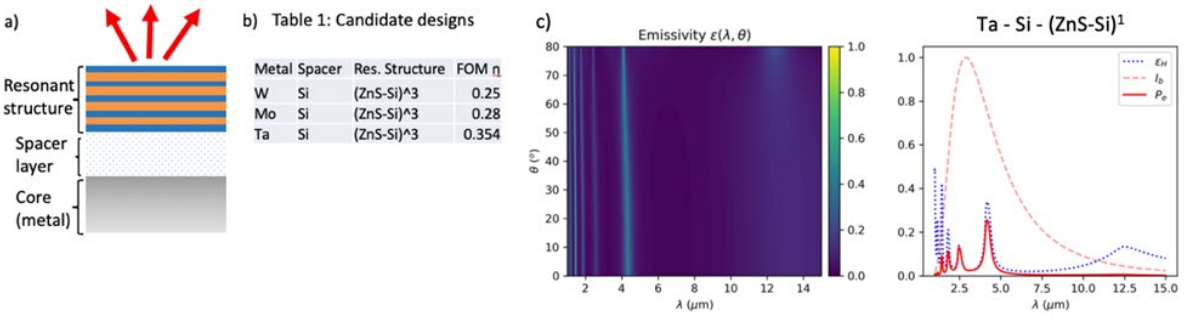

Figure 9. a) Candidate photonic designs for narrow-band thermal emission, inspired by photonic coupled-mode theory. b) Subset of results, varying materials for the core-spacer-pattern components. c) Example of a simple configuration with only three layers on top of tantalum core: Ta - Si - (ZnS-Si)^1. Plot of emissivity vs wavelength and incident angle, showing narrowband emission; Right: hemispherical emissivity (dotted blue), blackbody spectral intensity (dashed red), and the product of the two (solid red).

structure separated by a spacer layer. For a coupled-mode resonant system, it is analytically predicted that matching the external leakage rate (which depends on the resonant structure) with the intrinsic loss rate (which depends on the properties of the spacer layer), would give rise to narrow-band emission.

Motivated by the theory of narrowband thermal emission, we considered arrangements generally specified as *(core)-(spacer)-(pattern)*^{N}, where the materials and thicknesses of all layers are varied, and *N* is the number of pattern repetitions. Candidate spacer and pattern materials were selected for their potential for IR operation, including Al_2O_3, SiO_2, TiO_2, Si, ZnS. Analyzed core materials include refractory metals W, Mo, Ta. All permutations of these materials were considered, with *N*=1,2,3 number of repeating patterns. Operating temperature of 1,000K was assumed.

A subset of obtained results is shown in Figure 9**b**. Among the analyzed permutations, we found the combination of a tantalum core and a ZnS/Si pattern to be especially suitable. A *N*=3 repeating pattern shows η exceeding 0.35 (layer thicknesses: 140-183-442-334-484-281 nm). Interestingly, the simplest *N*=1 arrangement consisting of only three layers reaches η~0.31 (Figure 9**c**; thicknesses: 301-451-322 nm), which is superior to even *N*=3 arrangements for tungsten or molybdenum cores. The simplicity of this design could be relevant in practice. Our analysis revealed several key insights. For one, it is advantageous to use dielectric materials with low phonon-polariton absorptivity in the infrared, thus concentrating absorption (and consequently emission) only within the metallic core. In addition, parasitic emission outside the 4-4.5 um spectral range can be reduced with metal cores with low intrinsic background emissivity (e.g. Ta vs W). Temperature effects on intrinsic material properties are likely to be relevant. Finally, preliminary results with hafnia as the dielectric oxide material show potential for even higher efficiencies, owing to hafnia's transparent nature in the long-wave infrared part of the spectrum.

2.1.3 Epsilon-Near-Zero 1D Metamaterial

During the discovery phase of candidate coatings, a new structure consisting of a stack of alternating refractory materials (metal and dielectric) was designed to produce a metamaterial called an epsilon-near-zero (ENZ) coating [16]. The design tunes the real part of the dielectric constant parallel to the layers to be zero within the range of the desired effect, in this case, increased absorption and hence enhanced emittance at our target wavelength. The stack design is shown in **Figure 10**, which employs alternating subwavelength-thickness layers of SiC and TiN, with suitable properties to tune the emittance into the mid-IR.

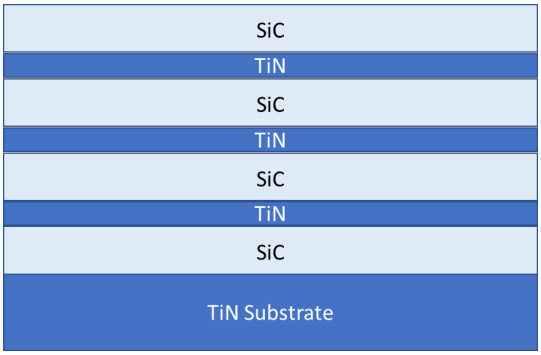

Figure 10. Refractory metal-dielectric ENZ metamaterial with alternating layers of SiC (330 nm) and TiN (30 nm).

The predicted emittance of this design is plotted versus wavelength in Figure 11 for both narrow-band response about the targeted emission wavelength of 4.2 μm as well as the broadband response. The resulting structure is not dependent on a resonance condition of the stack but rather the metamaterial properties provided by the alternating layers of SiC/TiN that tunes the ENZ frequency (plasma frequency) of the metamaterial.

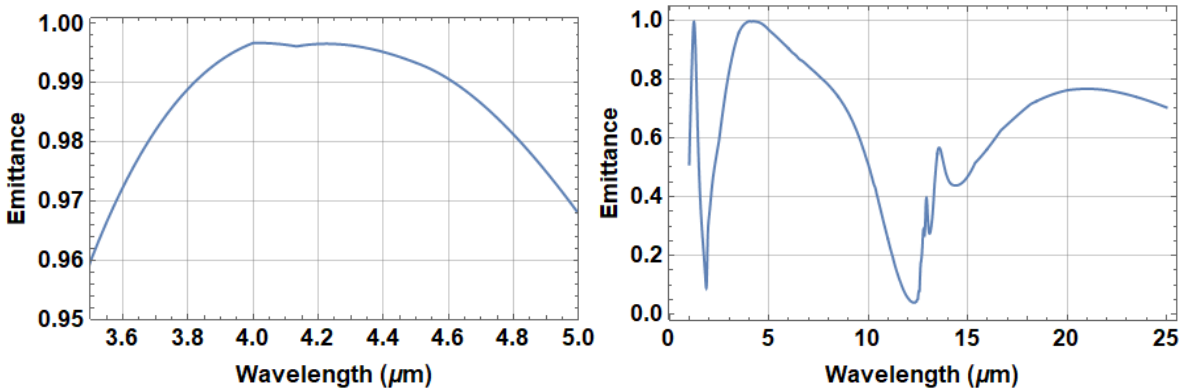

Figure 11. Plots of emittance versus wavelength are shown for the new metamaterial design consisting of 4 periods of alternating SiC/TiN layers over a narrow wavelength range (above left) as well as its broadband performance from 1 to 25 μm (above right). The dip in emittance at ~12 μm is caused by the reststrahlen bands of SiC.

Another advantage of the ENZ design is its relative insensitivity of emittance to angle of incidence for angles less than 45°, and this behavior showing emittance versus wavelength over several incident angles from 0° to 60° is depicted in **Figure 12**. Even at 60° incident angle, the emittance is still ~0.9 over the range from 4.0 to 4.5 μm.

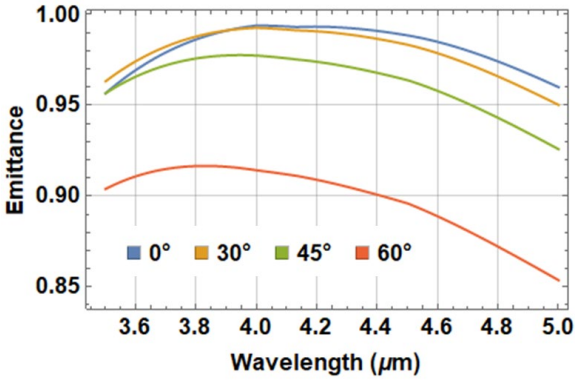

Figure 12. Emittance versus wavelength for angles of incidence ranging from 0° to 60° showing that although there is, especially for angles greater than 45°, a ~10% change in emittance, at those angles 45° or less the emittance exceeds 0.96.

Finally, a design must be manufacturable to be useful in practice. To probe this attribute, a sensitivity analysis was performed to plot emittance versus wavelength when the thickness standard deviation of the TiN layers is allowed to vary as much as 5 nm, and that of the SiC layers is permitted to vary up to 10 nm randomly for 100 trials. The results are shown below in Figure 13 and demonstrate that for fairly large deposition errors, a very serviceable selective emitter coating is still possible with emittance exceeding 0.9.

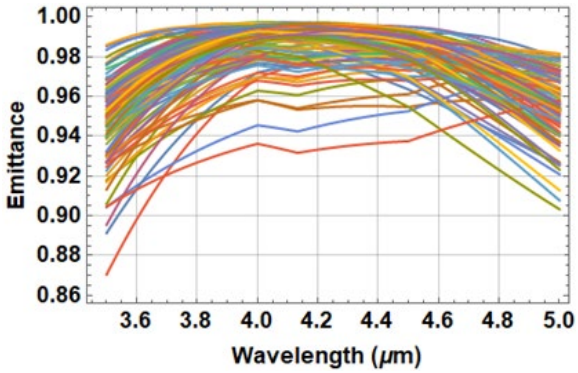

Figure 13. A sensitivity analysis to determine the effect on depositing layers that deviate in thickness from the design values was undertaken for 100 trials. TiN layer thickness varied by 5 nm, while the SiC layers could vary up to 10 nm randomly in thickness. The emittance still exceeds 0.93 at the center wavelength of 4.2 μm even with these deposition errors.

2.2 Photonic Crystal (PhC) Motif

The PhC motif offers a very large design space in terms of geometries of the subwavelength periodic structures that can induce excitations at a targeted wavelength in addition to choices of refractory materials from which to form the periodic structures. In this project, it was not possible to sample a very large number of candidate structures so work centered on a few designs where prior published work provided confidence in achieving selective emission at mid-IR wavelengths.

2.2.1 Cavities

This approach is modeled after Yeng et al., [17] where the structure consists of a periodic array of air-containing cavities having radius *r*, depth *d* and period *a* fabricated as a tungsten (W) monolith. The periodic structure gives rise to band gaps caused by destructive interference of multiple reflections of light propagating in the crystal at the interfaces of high- and low-dielectric constant regions. In this case, the cavities are assumed filled with air. Using the designs described by Yeng et al.[17] as the starting point, the parameters *r* and *d* were optimized to achieve the desired narrow-band emittance at 4.2 μm. A rendering of the structure taken from Yeng et al. [17] along with emissivity modeling results achieved using the RSoft FDTD software is shown in **Figure 14**.

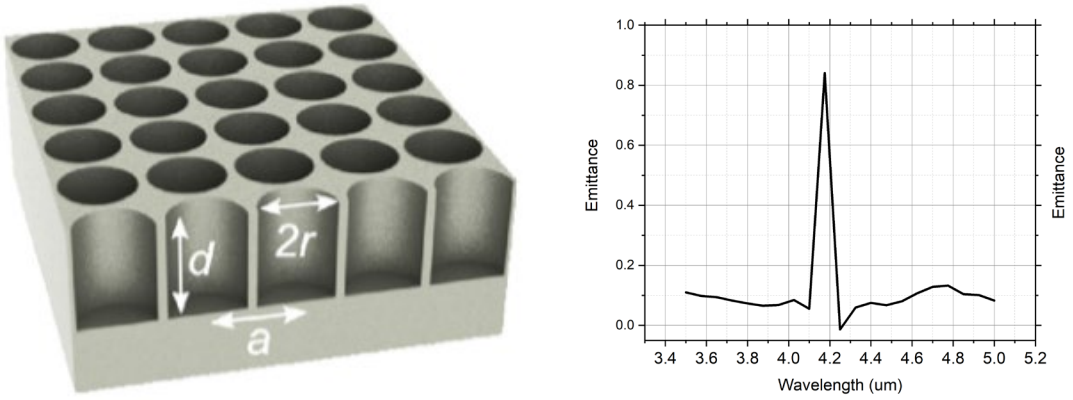

Figure 14. The 3D structure of the cavity-based PhC is shown (above left) taken from Yeng et al. *[17]* After the depth and radius variables were optimized, the emittance of the structure tailored to maximum emittance at the CO_2 line at 4.2 μm is shown in the above right frame.

The modeling approach used is the three-dimensional (3D) finite difference time domain (FDTD) method. FDTD offers an exact solution to Maxwell's equations and is applicable to arbitrary structures with feature size smaller than the wavelength of interest. In FDTD, the time derivative of the E-field and the curl of the H-field are solved in time steps on a 3D mesh. The FDTD program FullWAVE from Synopsys, Inc was used to perform the FDTD calculations. In the design shown in **Figure 14**, the optimized structure has dimensions or a cavity radius *r* of 1.6 μm, a cavity depth *d* of 5.6 μm, and cavity period *a* of 4.0 μm. Yeng et al. [17] fabricated a similar design using interference lithography (IL) where exposure of a chrome mask and reactive ion etching (RIE) were used to obtain the final structure.

Although this design is predicted to have an excellent emissivity profile, it has a serious drawback because the intended application here would inherently result in the cavities being filled with $scCO_2$. This would dramatically change the predicted emissivity profile from the one shown in **Figure 14** due to the very large difference in index of refraction between air and $scCO_2$. Although additional tuning of the structure might restore the emissivity profile, a further complication arises from the fact that photons emitted in the cavities would be largely absorbed by the $scCO_2$ causing localized heating. Moving this heat to the main fluid flow would necessarily involve relatively slow convective heat transfer in these small cavities. Since the core objective of this project is to improve the radiative heat transfer, we do not believe this design would result in any significant overall improvement in heat transfer efficiency in a real heat exchanger. A possible solution is to fill the voids with a material impermeable to $scCO_2$ and transparent in the mid-IR range. However, this approach would likely suffer from several fabrication challenges and thermal cycling instabilities that would need to be solved. Therefore, the cavity design option was not evaluated any further for this project.

2.2.2 Posts

An alternative to the method using a cavity structure is one that instead uses posts arrayed on top of a flat tungsten (W) substrate, which is a method originally suggested by Heinzel et al. [18]. A side view of the pattern and modeling results of emittance versus wavelength for this PhC is shown in **Figure 15**. The post-style PhC design results in a smaller aspect ratio structure with post height *h* of 2.8 µm (versus the 5.8 µm cavity depth), and post radius *r* of 1.6 µm (the same as the cavity design) as well as period *a* of 4.0 µm. This design may offer advantages in simpler and easier fabrication in that the posts may be deposited or grown. The additional exposed surface area and surface roughness would also be expected to enhance convective heat transfer to the main CO_2 flowing across the surface. However, the predicted emissivity of this structure is significantly below our target. Additional optimization is necessary to achieve our emissivity target. However, because this design utilizes a single material, it is expected to have no thermal cycling stability issues.

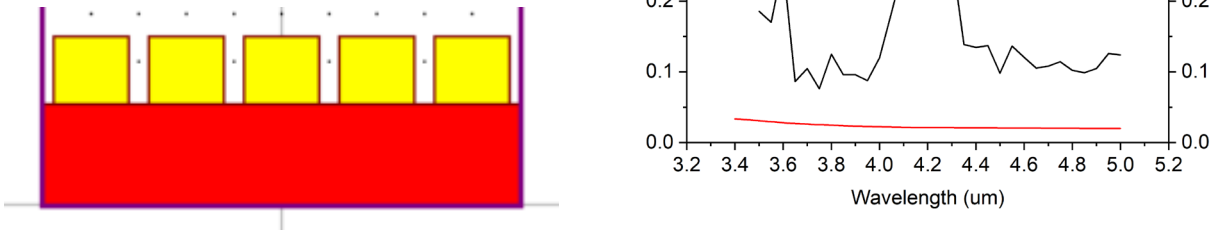

Figure 15. A side view of the post version of a PhC structure is shown (above left). The emittance as a function of wavelength (above right) is also shown for an optimized structure in which the radius *r* of the posts as well as their height *h* were optimized to maximize the emittance of the structure at the CO_2 wavelength of 4.2 µm. As was the case with the PhC cavity approach, the structure is a monolithic tungsten (W) structure. Also shown in the red trace of the emittance versus wavelength plot is the behavior of W metal, further illustrating the efficacy of the engineered PhC structure in providing narrow band, enhanced and tailored emittance.

Because the initial performance was not optimum, the photonic crystal (PhC) structure shown in **Figure 15** was examined to explore methods to achieve better performance. Here, the reference is to the post or pillar approach, which is the dual of the cavity PhC design that was introduced in Figure 14. A 4 X 4 array was constructed in the FDTD package FullWAVE but the computations use only one unit cell invoking periodic boundary conditions to reduce computation time. The posts have parameters of *d*, post height, *r*, post radius, and *a*, pitch or center-to-center spacing of the periodic array of posts. Two greatly improved designs resulted as shown in Figure 16. Parameters for the two designs are summarized in Table 1 below. With reference to the initial design (**Figure 15**), the emittance is improved by 37.5%.

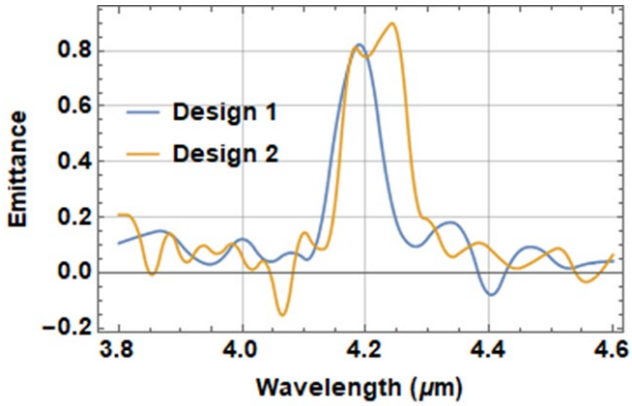

Figure 16. Emittance versus wavelength for the two improved post PhC designs.

Table 1. Summary of performance and parameters for the improved design for the post-type PhC design.

Design	Peak λ	Emittance	FWHM	a (μm)	r (μm)	d (μm)
Design 1	4.2	0.80	90 nm	3.8	1.65	2.3
Design 2	4.2	0.85	116 nm	3.9	1.7	2.1

The post design offers advantages when compared to the cavity PhC in that in addition to the enhanced emittance (radiance) due to the PhC surface, the post design may improve other modes of heat transfer. Like the cavity PhC design, the surface is only constructed of one material and potential issues caused by mismatched coefficients of thermal expansion of different materials are avoided. Finally, the post design may be amenable to additive manufacturing approaches so that scale up to larger surfaces may be simpler to implement.

However, additional analysis revealed some issues with the post design. When examining the emission of thermal radiation in the 4-4.5 μm range over a full range of emission directions, extensive parameter sweeps over unit cell dimensions revealed this configuration to be suboptimal for the STERADIAN emitter. While the requirement of narrowband radiation around 4-4.5 μm can be satisfied for emission perpendicular to the surface, this behavior does not persist for non-perpendicular emission (**Figure 17b**), which could affect the overall radiative heat transfer in a heat exchanger application.

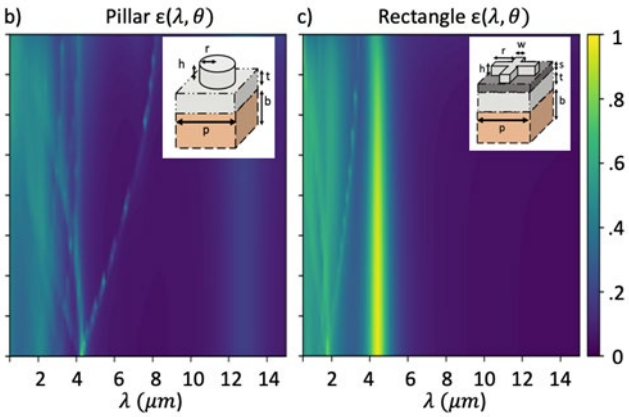

Figure 17. Two-dimensional photonic crystal motifs (pillars and rectangles): pillars can work well at normal incidence but exhibit angularly sensitive thermal radiation. A cross bar configuration maintains strong peak of emission in the 4-4.5 μm range over all emission angles and both polarizations.

2.2.3 Cross-Bar

To maximize desirable emission radiated in all directions, we identified a rectangular metallic slab configuration [19] as a potential candidate (**Figure 17c**). The principle of operation is based on the modal coupling between the exposed metallic top and the metallic core, separated by an insulating spacer. This configuration is

substantially superior at achieving narrowband thermal emission over a broad angular range and for both polarizations. **Figure 17c** shows polarization-averaged emissivity with a predominant peak in the 4-4.5 μm range (for a platinum core/pillar/slab, and silica dielectric spacer; dimensions: *p*=1.69um, *h*=80nm, *r*=570nm, *w*=580nm). Operating temperature of 1,000K was assumed.

Relative to optimized thin-film thermal emitters, the 2D photonic crystal slabs investigated show a stronger peak of radiation in the 4-4.5 μm range, but overall less efficient out-of-band thermal emission. This is attributed to a more pronounced parasitic emission below 4 μm, from the combination of the lossy metal core and higher-order resonances associated with the structure. We estimate that this parasitic emission could be reduced with metals that exhibit a lower intrinsic background emissivity. With a single metallic pattern and a single spacer layer (and overall thickness of ~200 nm), the 2D photonic crystal slab's simplicity of design could be advantageous from a practical standpoint.

Optimization of the cross-bar unit cell design was performed by focusing on two key parameters in the design: (a) identifying optimal constituent materials and geometry that maximize thermal emission design figure of merit, and (b) incorporating effective encapsulation for high-temperature operation. Previously, we discovered that a metallic core consisting of a material with low intrinsic emissivity is desirable (such as Cu).

Among additional configurations analyzed, particularly good optical performance was found in Cu-HfO_2 structures. The choice of Hf oxide (HfO_2) is motivated by its suitable optical properties in the infrared (e.g., low loss) and its well-known stability at high temperatures (e.g., through sintering with yttrium oxide to realize yttria-stabilized hafnia). **Figure 18a** shows a schematic of a unit-cell of interest, where narrowband thermal emission in 4-4.5 μm range arises as a resonance between the metallic cross bar and the metallic core separated by a dielectric coating. UMN staff systematically explored the parameter design space (including the cell period, cross bar height and width, and spacer thickness) through rigorous coupled wave analysis (RCWA) coupled to efficient nonlinear optimization framework and verified with the finite-difference time-domain (FDTD) method.

To guard against encroachment of debris or unwanted oxide growth, a protective encapsulation layer was incorporated in this photonic crystal design. This layer is intended to provide both abrasion protection to the underlying layers as well as chemical protection from any contaminants in the $scCO_2$ heat exchange fluid (such as water, oxygen, etc.) that could react with the

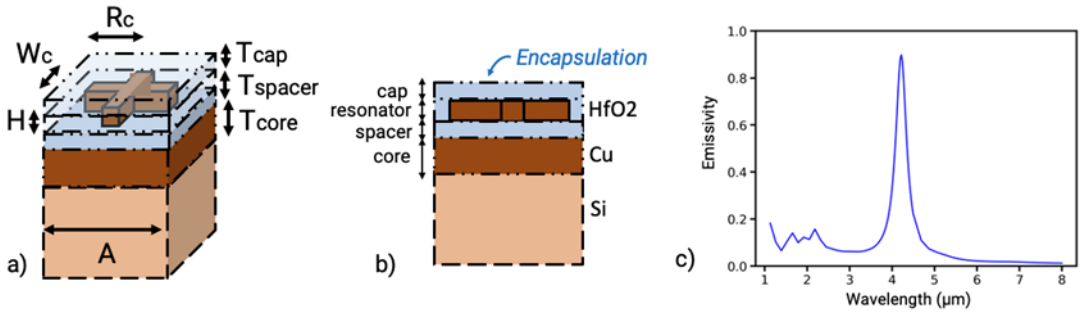

Figure 18. a) Encapsulated selective thermal emitter demonstrating narrowband emission. Characteristic design parameters are shown. b) Side-view shows hafnia (HfO_2) encapsulation as protection for operation in a hostile, elevated-temperature environment. c) Narrowband emission spectrum for an encapsulated design, optimized over a broad parameter space (details in main text).

underlying materials at high temperature. **Figure 18b** shows a side-view of the emitting unit cell with the encapsulant ("cap") film.

Generally, the presence of a capping/encapsulation layer modifies the thermo-optical properties of the emitter, which factors into the desired figure of merit. In our analysis, we showed we were able to quantitatively account and correct for the optical properties of the capping layer. The obtained candidate structure shows highly selective narrowband emission (**Figure 18c**, for $A = 1.72$ µm, $H = 53$ nm, $R_c = 0.36$ µm, $W_c = 0.17$ µm, and thicknesses $T_{cap} = 100$ nm, $T_{spacer} = 80$ nm, $T_{core} = 200$ nm) with $\eta \approx 0.43$, representing the best performing PhC design produced by this project. The cap layer thickness in a practical coating will depend on several other considerations beyond optical parameters and could be adjusted to meet these additional requirements. Importantly, the team found that the cross-bar morphology is not very sensitive to the thickness of the encapsulant. The physical explanation stems from the fact that the resonant mode is localized in the gap between the metallic core and the metallic cross bar and not in the immediate vicinity of the encapsulant. In conjunction with the benefits of broadband angular emission and an ultrathin form factor, this behavior further strengthens our finding that a cross-bar emitter configuration is a promising candidate for STERADIAN applications.

2.3 STERADIAN Coating Design Summary

Two distinctly different design approaches (structural motifs) were considered for SECs during the project to achieve the project goals: thin film and PhCs. The thin film motifs investigated included DBRs, coupled-mode, and epsilon-near-zero refractory 1D metamaterial. The PhC motifs considered cavities, pillars, and cross-bar configurations. Each design offers advantages and disadvantages in terms of optical properties, thermal cycling robustness, and manufacturing scalability. Additional work is needed to more adequately assess these tradeoffs to determine preferred designs for commercial application.

Irrespective of SEC design, experimental validation is necessary to confirm the validity of the predicted emissivity of these coatings. Both modeling methods (FDTD and TMM) are reliable but depend on the accuracy of the material dielectric constants used by the algorithms. Although the metals and dielectrics used in the designs have well-characterized thermal and optical properties, high-temperature dielectric and index of refraction data are scarce and challenging to obtain. Thus, actual emissivities at high temperatures may deviate from the predictions in this report. Also, numerical modeling has pitfalls such as sampling and other details that must be eliminated through sensitivity analyses. Finally, any candidate design must be subjected to a rigorous tolerance analysis to ensure that the resulting structures' performance can be met based upon the sources of error in the chosen fabrication route.

3.0 Selective Emitter Fabrication

As discussed in the preceding section, several selective emitter coating (SEC) materials were identified that have the potential to emit IR radiation within a narrow wavelength range of 4-4.5 µm. In this section, details on fabrication of the two most promising SEC candidates, the TPP-based DBR structure and a cross-bar array PhC structure, are provided. Electron beam evaporation and sputter coating were used as the primary fabrication techniques for constructing the layered DBR structures, while nano-patterning techniques such as stepper lithography and electron beam lithography were used to produce the PhC structures.

3.1 DBR Structure Fabrication

Initially, SEC synthesis was focused on a simple layered structure composed of TiN (2,000 Å), SiC (3,300 Å), HfO_2 (6,500 Å), and a capping layer of 1000 Å SiC layer. The deposition was carried out on BK-7 glass or Si wafers using a DynaVac system setup to perform electron beam evaporation and sputter coating. The base pressure of the system was $<2 \times 10^{-7}$ Torr, while the working pressure during each sputtering process was adjusted to maintain the lowest possible value to sustain a plasma discharge. Initial deposition trials used Hf, Ti, and Si cathodes for the fabrication process. **Table 2** below highlights optimization of several parameters, including gas composition, power settings, and duration to establish coating parameters for each individual layer. The thickness of these coatings was then analyzed using a physical profilometer (Alpha Step).

Table 2. Parameters used for SEC deposition

Material	Gas	Duration	Pressure, mTorr	Thickness, (Å)	Parameters	Substrate
Hf	Argon 100%	20 min	5.0	1,120	56A/min 71.5 watts	BK-7 glass
HfO_2	Ar/O_2 50/50	20 min	5.0	630	31.5A/min 98 watts	BK-7 glass
Hf	Ar 100%	60 min	4.0	4,850	80.0A/min 94 watts	BK-7 glass
HfO_2	Ar/O_2 55/44	60 min	4.9	580	9.7A/min 97 watts	BK-7 glass
HfO_2	Ar/O_2 55/44	180 min	6.0	2,150	12A/min 163 watts	BK-7 glass
HfO_2	Ar/O_2 55/44	90 min	5.0	2,545	28.3A/min 195 watts	BK-7 glass
TiN	Ar/N_2 50/50	180 min	4.5	3,500	19.4A/min 235 watts	BK-7 glass
TiN	Ar/N_2 50/50	9 hours	4.5	5,810	10.75A/min 230 watts	BK-7 glass
TiN	Ar/N_2 50/50	18 hours	4.0	19,000	17.6A/min 238 watts	BK-7 glass, Si
TiN	Ar/N_2 60/40	9 hours	4.0	11,900	22A/min 231 watts	BK-7 glass, Si
SiC	Ar 100%	3 hours	3.5	6,800	38A/min 270 watts	BK-7 glass, Si

Deposition of TiN films during the above optimization trials were initially performed by sputtering Ti in a nitrogen atmosphere at room temperature. However, this did not yield the desired stoichiometry and the Ti metal target was later switched for a TiN target, which yielded a TiN coating thickness of ~2,300 Å (after 30 minutes at ~250 watts). Based on these results, the first batch of DBR samples were prepared that included four layers, namely TiN 2,000 Å, SiC 3,300 Å, HfO_2 6,500 Å, and a final capping layer of SiC (1,000 Å). The first run utilized a variety of substrates, including glass (25 x 25 and 25 x 75 mm, and one 15 mm Si wafer. Surface profilometry of the prepared films revealed a total coating thickness of ~12,100 Å, similar to the theoretical thickness of 12,800 Å.

Unfortunately, XRD analysis of the prepared coatings revealed the presence of a Hf metal layer (reflections at ~33°, 35°, and 37° 2θ), instead of the desired HfO_2 layer (**Figure 19**). In light of these findings, the sputter coating system was reconfigured to accommodate a substrate heater that can reach 400°C. Sputtering Hf metal in the presence of O_2 at elevated temperatures has been demonstrated to produce HfO_2 layers. However, in addition to using Hf metal targets, a HfO_2 target was also acquired to allow direct sputtering of HfO_2, which is also a known pathway to producing crystalline coatings of HfO_2.

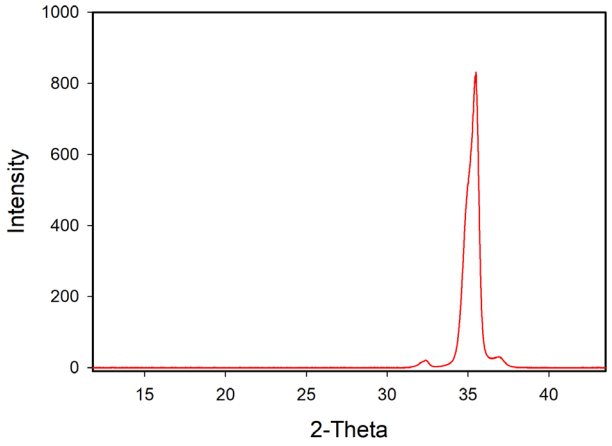

Figure 19. X-ray diffraction tracings of the DBR coating produced in Run #1 (Figure 6a). The reflections are assigned to Hf metal (PDF 05-0670).

Using the HfO_2 target, two sets of layered DBR samples were prepared (02-22-21 and 02-24-21) and characterized by focused ion beam (FIB) scanning electron microscopy (SEM) techniques. **Figure 20** shows cross-sectional analysis of the materials and reveal very well-defined interfaces in the materials. Gratifyingly, thickness measurements using SEM show that the HfO_2 layer was very close to the targeted 650 nm thickness. However, both the TiN and SiC layers were found to be thicker than targeted values.

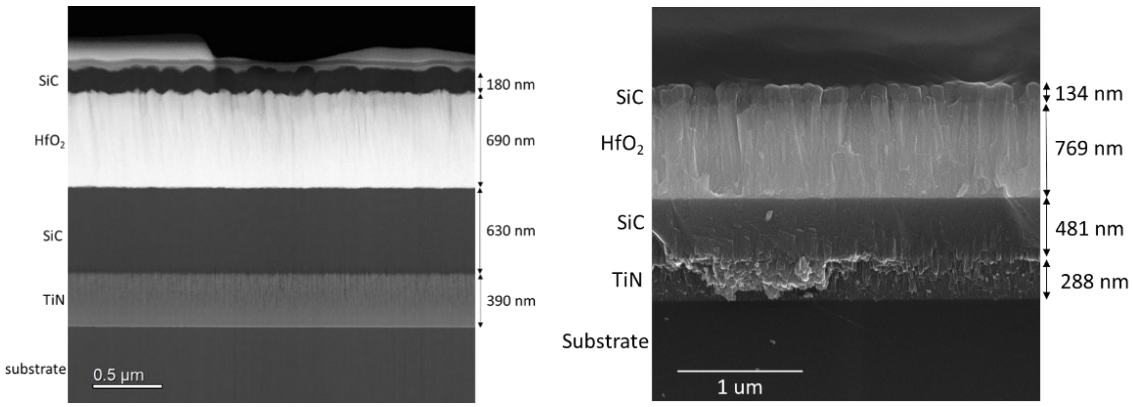

Figure 20. Cross-section view of DBR samples prepared on 02-22-21 (left) and 02-24-21 (right).

The second fabrication, 02-24-21, was conducted with modified deposition times for the TiN and SiC layers and characterized by scanning electron microscopy (SEM). As shown in **Figure 20**. Cross-section view of DBR samples prepared on 02-22-21 (left) and 02-24-21 (right)., the TiN and SiC layers were all reduced in thickness compared to the initial 02-22-21, however, both the TiN and SiC layers remained between 34 and 46% too thick. In addition, the HfO_2 layer saw a slight increase in thickness (18%). Based on these results, additional DBR sample sets were prepared on 03-02-21 and 03-05-21 and were used for emissivity measurements (see Section 4.0).

Characterization of the DBR samples (03-02-21 and 03-05-21) was performed using SEM analysis of cross sections revealing the thickness of each later. **Figure 21** shows the individual layer thicknesses for both samples, which have an overall thickness of 1.36 µm (03/02/21) and 1.58 µm (03/05/21). Although still deviated from the target design, the measured thickness, specifically for the 03-02-21 sample, is closer to the desired thickness for the DBR materials.

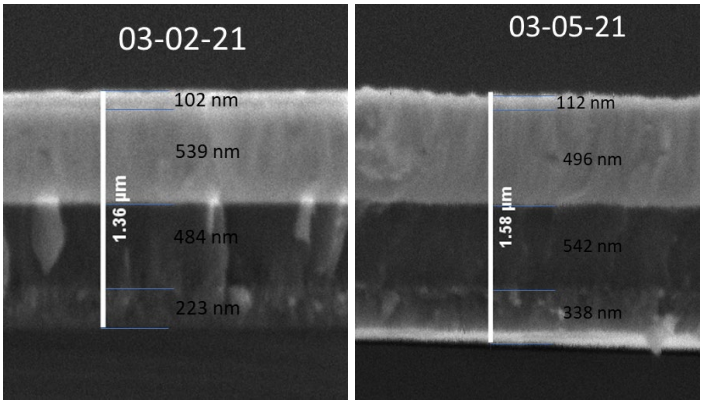

Figure 21. Cross-section view of DBR samples prepared on 03-02-21 and 03-05-21.

After fabrication, the reflectance of the film was measured to estimate emittance as, $\varepsilon = (1-R)$ for an opaque material. The measured film parameters were then entered into the thin film modeling software and showed good agreement with measured properties. Plots below show of the measured emittance along with the as-built parameters shown in **Figure 22** modeled by the thin film software.

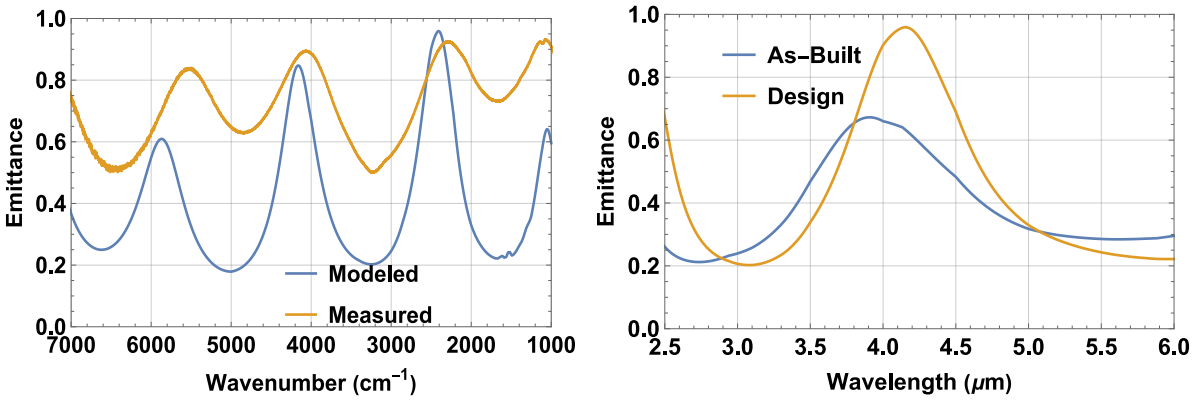

Figure 22. Plots showing modeling results of the as-built DBR/TPP design using high temperature SiC and HfO_2 in wavenumber space (above left) and plotted as a function of wavelength (above right) in microns. The design center wavelength is 4.2 µm.

These plots show validation of the ability to fabricate a thin film, measure its reflectance, and using measured properties of each material layer via SEM, model its performance with good agreement in comparison with measured data.

3.2 Cross-bar PhC Fabrication

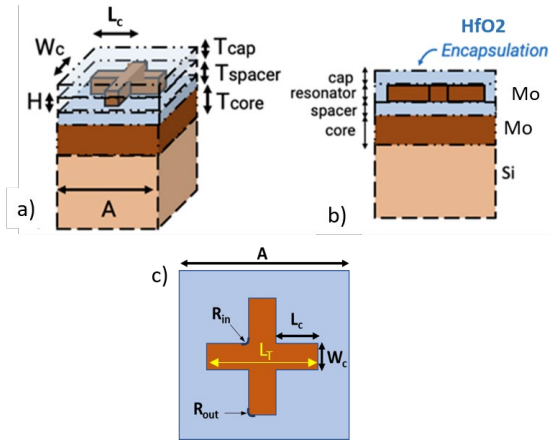

Figure 23. Cross-bar PhC target design.

To fabricate the cross-bar PhC designs (**Figure 23**), stepper lithography and electron beam lithography techniques were used in collaboration with the Washington Nanofabrication Facility (WNF) at the University of Washington. The fabrication process was initiated by coating 100 mm Si wafers with Mo (200 nm), HfO_2 (80 nm), and finally an additional Mo layer (71 nm). This was done in a Lesker Lab 18 sputter system capable of depositing both molybdenum and hafnia without breaking vacuum. The thickness of the molybdenum layers was measured using optical profilometry (Dektak XT) on masked wafers. The deposition rate of molybdenum was calculated to be 0.38 nm per second, when using a 350W Ar plasma operating at 10 mT. Therefore, a deposition time of 582 seconds was chosen for the the 200 nm core layer, while 190 seconds was required for the top Mo layer (71 nm). The hafnia spacer layer was deposited in a similar way except the thickness measurements were performed using a Woollam apha-SE ellipsometer. The deposition rate was measured to be 1.99 nm/min, when a 120W Ar plasma was used operating at 5 mT. Thus, a total deposition time of 41 minutes was used for the target design of 80 nm. These wafers were then used for cross-bar fabrication using stepper and e-beam lithography techniques described below.

A molybdenum etch protocol was also developed at the WNF. The etches were performed utilizing fluorine chemistry in an Oxford ICP etcher. The etch protocol etched molybdenum at 250 nm per minute and hafnia at 5 nm per minute, and has a selectivity of molybdenum to photoresist of 0.5.

3.2.1 Stepper Lithography

Table 3. Target dimensions for PhC fabrication.

Layer (top down)	Material	Label	(nm)
Cap	HfO_2	T_{cap}	100
Resonator Cross	Mo	H	71
		W_c	150
		L_c	344
		L_T	838
Spacer:	HfO_2	T_{spacer}	80
Core:	Mo	T_{core}	200
Substrate:	Si	T_{sub}	n/a

Using the parameters highlighted in **Table 3**, deep-UV stepper lithography was performed at the University of California, Santa Barbara using an ASML 5500 DUV Stepper. Optimization of fabrication parameters such as exposure time, fluxes etc. generated a set of 25 cross-bar PhC templates. However, the fidelity to the cross-bar design parameters was found to be impacted by rounding of the cross bar edges. To ascertain the impacts on the predicted emissivity, UMN re-modeled the emissivity of the 25 designs using a refined grid to capture the rounded features accurately in the model. While most of the patterns showed blue shifts away from our target 4.2 µm, the predicted emissivity spectrum of sample R1C7 showed remarkably good performance (see **Figure 24**), nearly matching the emissivity of the idealized cross bar design. Consequently, R1C7 was chosen as a final design pattern to be produced via stepper lithography.

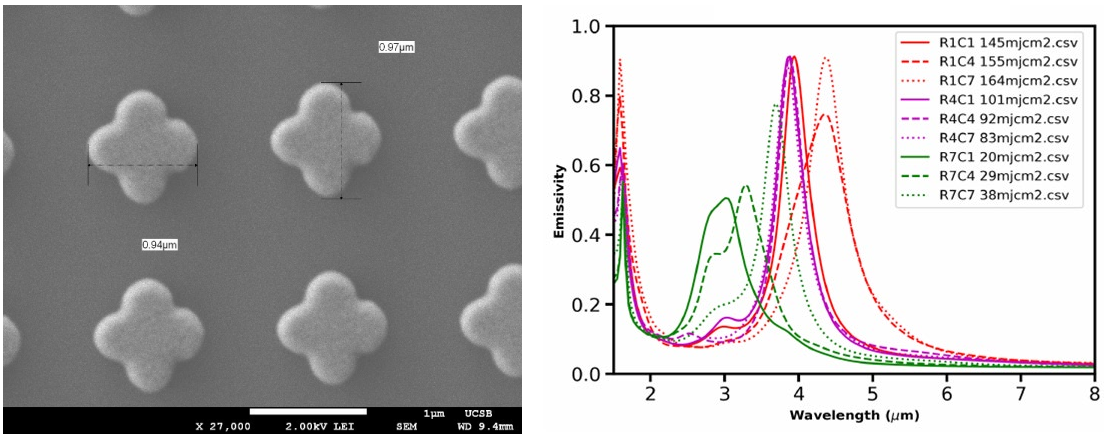

Figure 24. a) SEM image of stepper lithography template (R1C7) prior to etching for producing a 1 cm x 1 cm STERADIAN coated sample. b) Predicted emissivity profiles of selected stepper lithography samples.

In order to fabricate the R1C7 design, 60 nm of DUV42P-6 anti-reflection coating was first spun on the Mo/HfO_2/Mo wafers. Then, 500 nm of UVN30-0.8 resist was spun onto the wafers and baked. Following this, the wafers were exposed in the UCSB ASML stepper, which was followed by a post-exposure bake. Samples were then developed for 1 minute in a AZ300MIF developer, and oxygen etched for another minute to remove the anti-reflection coating.

Unfortunately, it was found that our etching conditions not only resulted in the shrinkage of the cross-bar features but also in the development of a residual ring around the structures (see **Figure 25**). Reflectance measurements were carried out on the post-etched sample to test the resultant effects on emissivity (seer Section 4.0). Improvements to the etching protocols are required to generate PhC structures that meet design specifications. Moreover, to generate a less-rounded cross structure, a new reticle with optical-proximity-corrected features will need to be developed. This in addition with more optimization runs to determine the proper feature sizes on the mask are expected to produce the correct feature sizes post etching.

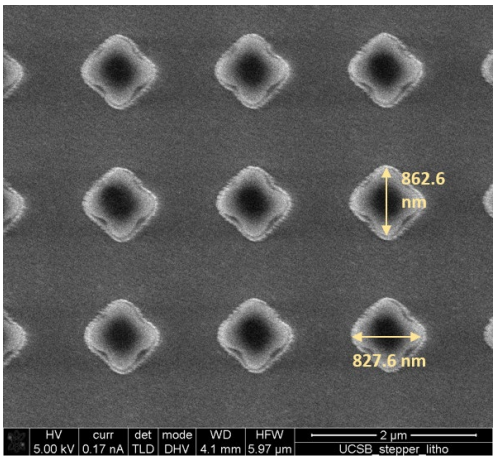

Figure 25. SEM image of post-etched PhC fabricated using stepper lithography

3.2.2 Electron Beam Lithography

As seen in **Figure 24**, the best samples prepared using stepper lithography still showed significant rounding of the cross-bars, which was related to the resolution limits of the technique itself. To obtain better cross-bar fidelity to the original design, electron beam lithography efforts were also undertaken at the WNF. For the fabrication, the Mo/HfO_2/Mo wafers were spin-coated with 230 nm of ma-N resist and baked. These were then exposed using the JEOL-JBX-6300FS Electron Beam Lithography system at the WNF. The total time required to write a 1 cm x 1 cm pattern on the Si wafer was approximately 20 hours, following which the wafer was developed using AD-10 for 2 minutes prior to etching. **Figure 26** shows an SEM image of the cross-bar structural design highlighting the high accuracy of the technique.

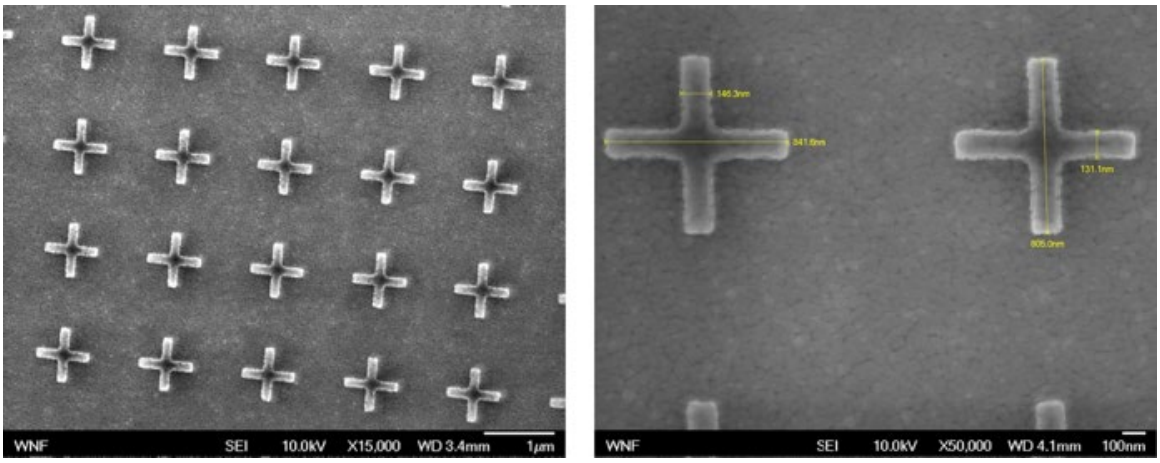

Figure 26. SEM images of E-beam lithography test sample (prior to etching) to reproduce cross-bar PhC design

The resist material was then etched by soaking in acetone overnight, followed by a 1 minute oxygen plasma etch in a Yield Engineering Systems downstream plasma asher. SEM images of the sample before and after oxygen plasma etching are shown in (**Figure 27**). Unfortunately, as can be seen in **Figure 27**, the etching steps degraded the continuity of the cross-bar structures resulting in separated grains about 5 to 50 nm in diameter. Although we have not done any simulation work to assess impacts on emissivity, these discontinuities almost certainly produce undesired polariton scattering and out-of-band excitations that will degrade the desired mid-IR emission properties.

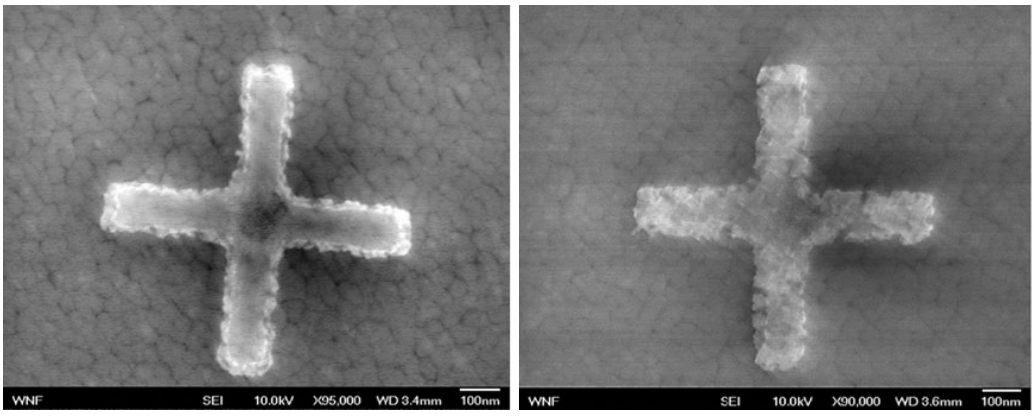

Figure 27. SEM images of E-beam lithography test sample before (left) and after(right) oxygen resist stripping

4.0 Emissivity Measurements

4.1 Instrument Design and Development

Infrared emissivity spectra of fabricated SECs (see Section 3.0) were collected at temperatures up to 800°C. Staff conceptualized and designed an apparatus for carrying out these measurements. Such a capability was envisioned to require two blackbody radiators, a translational stage, a 90° off-axis parabolic mirror, and a means to mount these items to an infrared (IR) spectrometer (**Figure 28**). One "background" blackbody would be dedicated to collecting background emittance spectra at a target temperature. The other "sample" blackbody would be used to heat a selective emitter to the target temperature to collect emittance spectrum of the emitter. A translational stage would be designed to maneuver either blackbody in front of a 90° parabolic mirror, which will reflect the IR radiation into the external source port of a Bruker Vertex 80V infrared spectrometer.

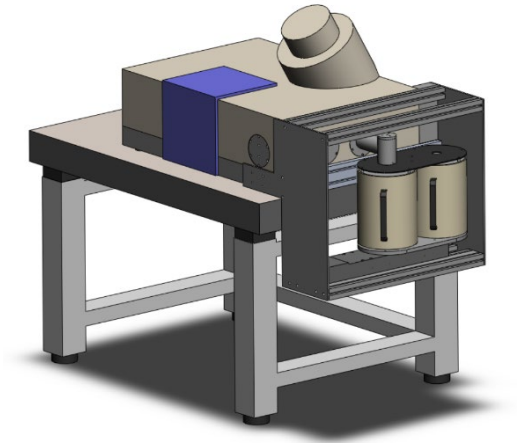

Figure 28. Emissivity apparatus connected to the IR spectrometer. Two blackbodies are mounted on a translational stage. Light is directed from either of these IR sources, through a KBr window to a parabolic mirror that is under the vacuum of the spectrometer, and finally towards the spectrometer's interferometer.

First, a custom enclosure/mount was designed and built to attach the translational stage (Model M-ILS250BPP from Newport) with the blackbodies (Model IR-564 with IR-301 Controller from Infrared Systems Development) to the spectrometer. This enclosure/mount was designed to withstand the nearly 30 kg mass of the stage and blackbodies while keeping the spectrometer rigidly linked and aligned, and the entire assembly vibrationally isolated using the optical table. Top and bottom yoke plates were designed and machined to bind the blackbodies together and mount them to the stage. To focus the emitted IR radiation from the blackbody cavity into the source port of the IR detector, a 90° parabolic mirror with a 4" focal length was acquired. This was mounted using optical components that would allow X, Y, Z translation, rotation, and tilt degrees of freedom and was optimized such that the signal at the detector was within better than 5% when either blackbody was positioned under the parabolic mirror.

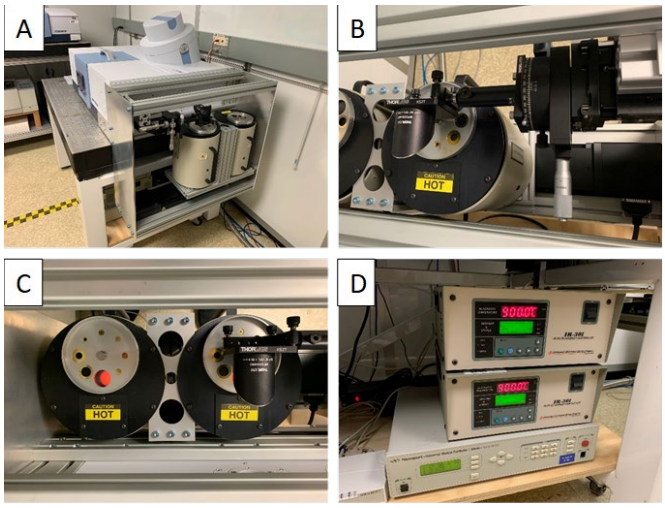

Figure 29. (A) Emissivity apparatus connected to the IR spectrometer. (B) Parabolic mirror and mirror mount. (C) Downward view looking at the two blackbodies mounted on the translational stage. (D) Blackbody temperature controllers and the controller for the translational stage.

A ceramic sample mount equipped with a thermocouple was initially designed to accommodate a 1.5 mm diameter 0.35 mm thick wafer substrate for the selective emitter (**Figure 30**). However, it was later determined that a holder entirely made from platinum would be necessary, as ceramic proved to be too brittle. Such a holder, along with a platinum sample platter was machined. Quantitative emittance measurements would also require that the light path from the "background" blackbody for the background spectrum match the light path from the selective emitter within the "sample" blackbody. Specifically, this means that the "background" blackbody should use a sample holder with a sample that emits blackbody radiation; in other words, the "background" blackbody should include a "secondary blackbody" sample. For this purpose, we machined an identical sample holder for the "background" blackbody that holds a cup of silicon carbide (SiC) nanoparticles. SiC was chosen due to its thermal stability and ability to emit blackbody radiation at temperatures up to 800°C and higher.

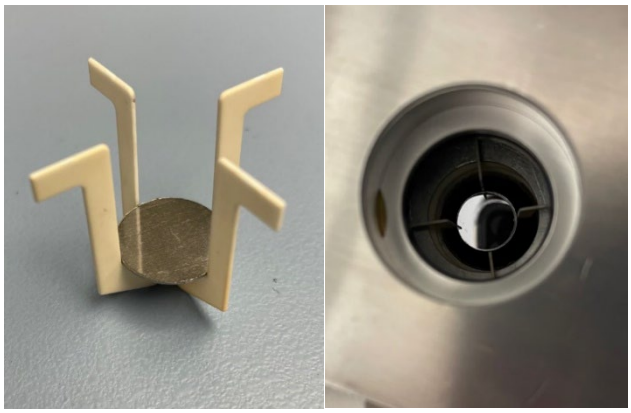

Figure 30. Ceramic sample holder with platinum platter.

The IR emissivity system was tested by collecting spectra of two mineral standards, forsterite (Mg_2SiO_4) and kaolinite ($Al_2Si_2O_5(OH)_4$), to confirm that the apparatus was performing as anticipated. Here, background emissivity spectra were collected with the platinum platter in place, and sample spectra were collected of the mineral powder spread on the platter surface. The emission spectra (**Figure 31**) for kaolinite at 400°C and forsterite at both 400 and 900°C were collected and compared to absorbance spectra collected using an attenuated total reflection (ATR) IR cell at 50°C. The emittance was computed with reference to the Pt holder background for comparison with previously reported values.

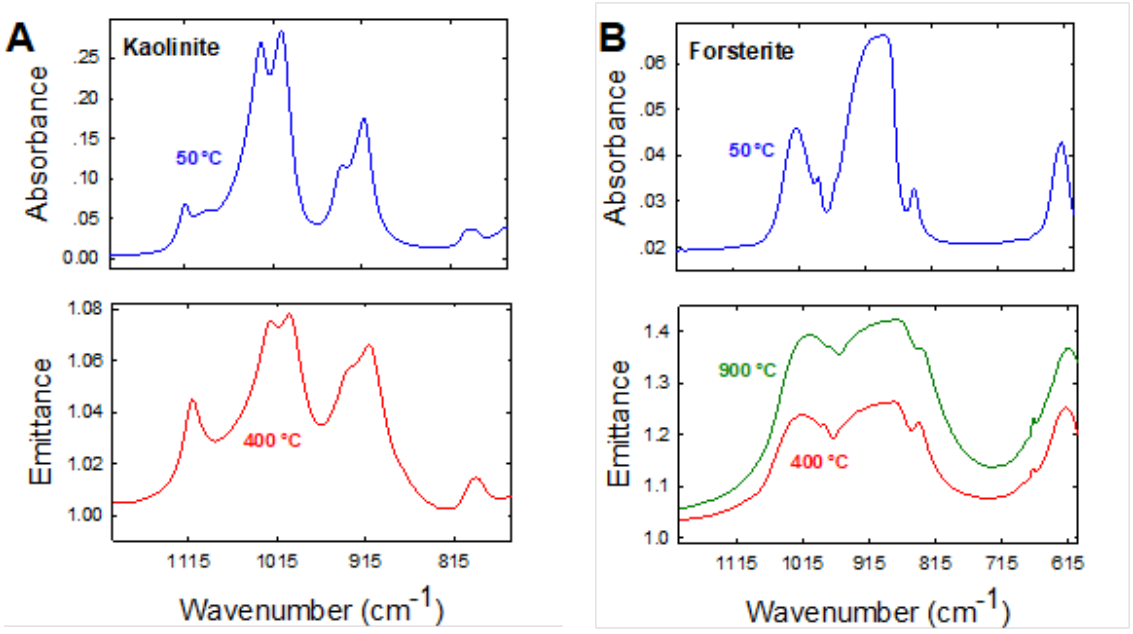

Figure 31. Emissivity and ATR absorbance spectra of (A) kaolinite and (B) forsterite

As a final addition to the capability, parts for enabling a nitrogen gas purge were designed and machined. This was done to prevent features arising from gas-phase CO_2 in the emittance spectra, which would otherwise overlap with the targeted 4.2 μm peak.

4.2 Infrared Emissivity Measurements

Infrared emissivity spectra were collected at 25°C on four DBR samples described in Section 3.1.1 (designated according to the date they were prepared: 02-22-21, 02-24-21, 03-02-21, and 03-05-21) using a Mid-IR integrating sphere for measuring reflectance (R). The emittance spectra are calculated as (1-R) and are shown in **Figure 32**. All four DBR samples prepared were attempts at producing a thin-film stack with the following spacing from bottom to top: Si-substrate-TiN (200 nm)-SiC (330 nm)-HfO_2 (650 nm)-SiC (330 nm). However, as shown in Section 3.1.1, the as-prepared thicknesses were significantly different from the design target. Our goal was to create a selective emitter with a peak maximum between 4 and 4.5 μm. While the emitter prepared on 02-22-21 badly missed this goal, the peak of the emitters prepared on the latter dates were within 1 μm of the target and demonstrates a progression towards our goal.

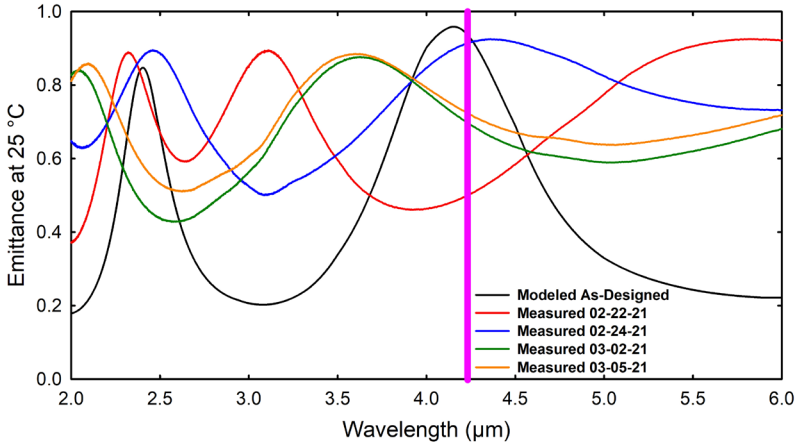

Figure 32. Emittance spectra of selective emitters measured at 25°C using an IR integrating sphere. Also shown is the modeled spectrum of the as-designed selective emitter.

Figure 33 and **Figure 34** are plots of as-designed, measured, and microscopy-data modeled spectra for emitters prepared on 02-22-21 and 02-24-21, respectively. Unexpectedly, the modeled spectra based on the SEM measurements demonstrated no better agreement with the measured samples. Also shown in **Figure 33** is an emittance spectrum at a conservative

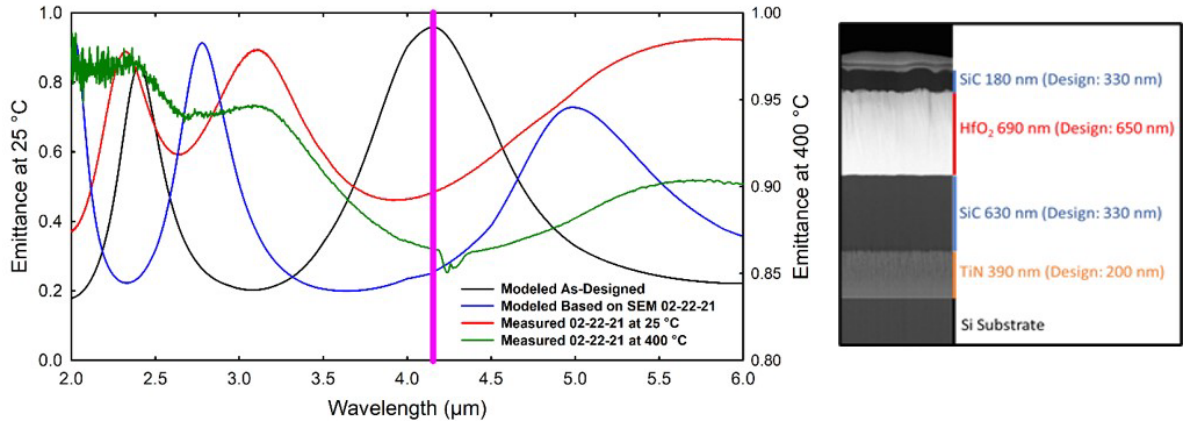

Figure 33. Emittance spectra of a selective emitter prepared on 02-22-21 measured at 25°C using an IR integrating sphere and at 400 °C using the high temperature IR emittance apparatus. Also shown are the modeled spectra of the as-designed selective emitter and based on DBR layer spacing measurements based on an SEM image of the emitter (shown to the right of the plot of the spectra).

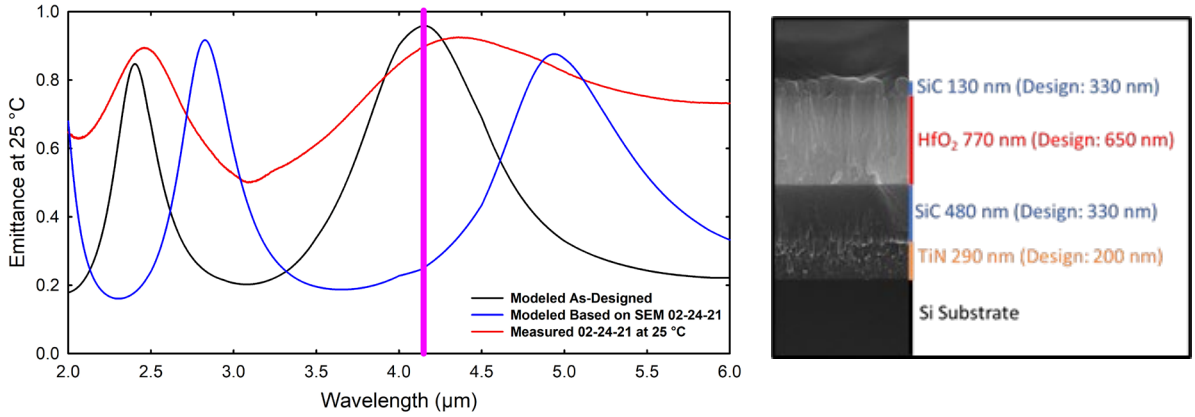

Figure 34. Emittance spectrum of a selective emitter prepared on 02-24-21 measured at 25°C using an IR integrating sphere. Also shown are the modeled spectra of the as-designed selective emitter and based on DBR layer spacing measurements based on an SEM image of the emitter (shown to the right of the plot of the spectra).

temperature of 400°C using the high temperature IR emissivity apparatus. This spectrum was collected before modifications mentioned above, so the N_2 purge was not operational; thus, visible at 4.2 μm is a feature due to gas phase CO_2 in the air. The wavelengths of the peaks and troughs in the spectrum collected at 400°C are in good qualitative agreement to those in the spectrum collected at 25°C. However, as indicated by the scale of the right-hand axis, the absolute emittance does not match the predicted as-designed spectrum, as well as the emittance spectrum collected at 25°C.

Emittance spectra was collected on three DBR samples (02-22-21, 02-4-21, and 03-05-21), at 800°C, and is shown in **Figure 35**. While none of the samples still matched the theoretically predicted targets, Figure 10 demonstrates that the emittance spectra measured at 800°C were now in much better quantitative agreement with those spectra measured at 25°C. Specifically, emittance values at 800°C were now less than a factor of 2 difference from those measured at 25°C, compared to a factor of 10 seen previously.

Last, the cross-bar PhC structures that were fabricated by the WNF using stepper and electron beam lithography (see Section 3.1.2) were examined. IR spectra were collected on the samples using a Mid-IR Integrating Sphere accessory. The spectra were measured as reflectance (R) spectra, and were converted to emittance (E) by E=1-R. While the spectra from the e-beam lithography sample was mostly featureless, the stepper lithography sample shows a broad emittance peak centered around 4.2 μm, that is absent in the "as-coated" Mo/HfO_2/Mo wafer (**Figure 36**). Previous published literature using similar cross-bar PhC designs shows that selective emission is achievable with these structures. Unfortunately, the degradation in the fidelity of the lithography samples prepared in this project (finished right before the end of the project) most likely resulted in the poor measured selective emittance performance relative to predictions.

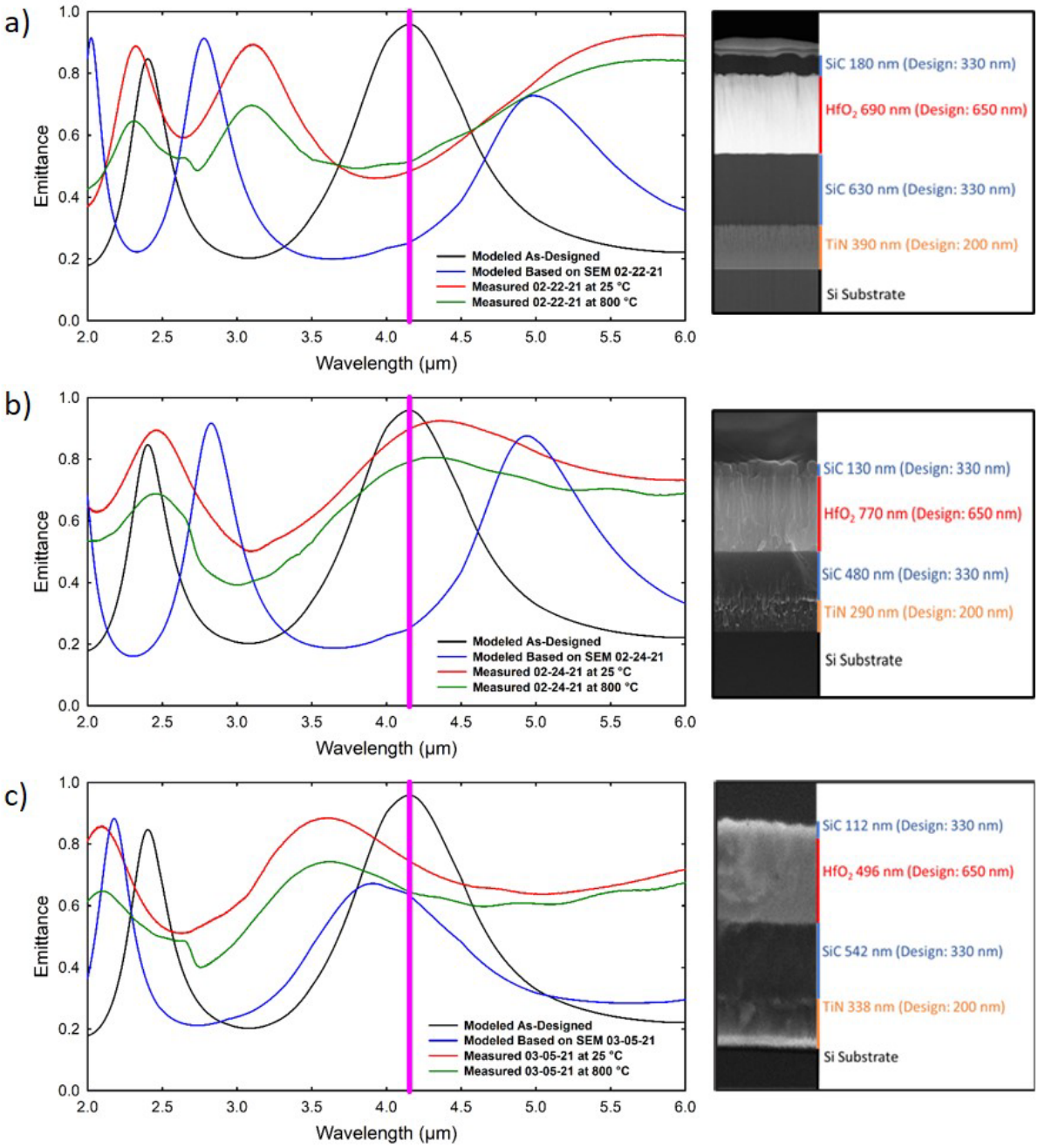

Figure 35. Emittance spectra of a selective emitter prepared on (a) 02-22-21, (b) 02-24-21, and (c) 03-05-21 measured at 25°C using an IR integrating sphere and at 800°C using the high temperature IR emittance apparatus. Also shown are the modeled spectra of the as-designed selective emitter and based on DBR layer spacing measurements based on an SEM image of the emitter (shown to the right of the plot of the spectra).

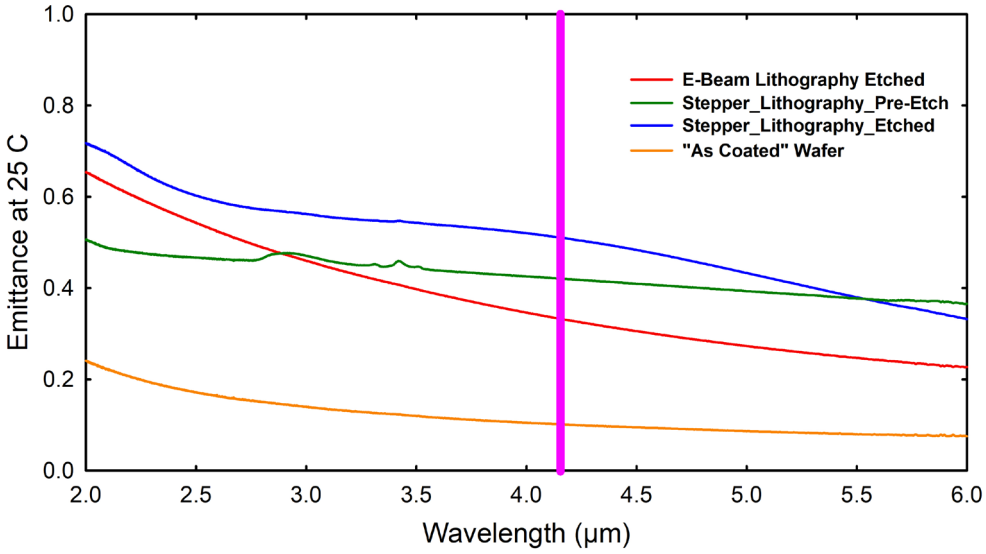

Figure 36. Emittance spectrum of a selective emitter prepared using electron beam lithography and stepper lithography (Refer to Section 3.1.2).

5.0 Impacts on Heat Exchanger Design

To assess impact on heat exchanger performance and size with our selective emitter coating, a numerical analysis was completed using ANSYS Fluent R18.2. A conformal quad-mesh of a counter-flow heat exchanger was generated with 1m x 1mm fluid channels separated by a 1 mm thick steel plate as shown in Figure 3. A generic heat transfer fluid was given properties of molten salt with temperature dependent thermophysical properties. Salt decomposition temperature was disregarded for this analysis.

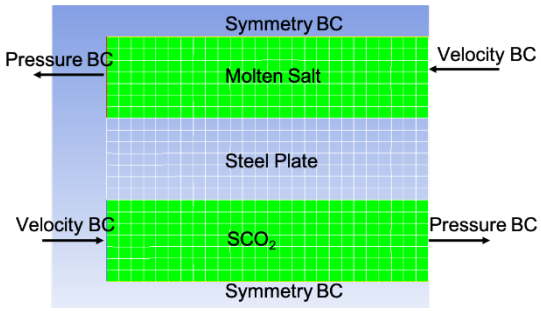

Figure 37. 2D Computational domain with boundary conditions (inlet of 1 m long counter-flow HX)

Radiative heat transfer was treated with the Discrete Ordinance (DO) model built into Fluent. The DO model is a robust method for solving radiative heat transfer problems that spans the entire range of optical thickness. The model solves for surface-surface radiation with a participating medium ($scCO_2$), gray and non-gray radiation with a large number of bands, scattering, anisotropy, and spectral wall emissivity. The model has been used by various researchers for radiation heat transfer with a participating medium [8, 20].

Figure 4 shows a comparison of heat exchanger length required to achieve 85% of the source inlet temperature for simulations run with and without a selective emitter. The results show a progressively increasing effect of radiative heat transfer with increasing source temperature as would be anticipated. We also found a nearly 25% reduction in heat exchanger size when coated with a selective emitter as source temperatures exceed 1000 K. It is important to recognize that these calculations represent a minimum level of improvement given the highly idealized nature of the heat exchanger used in this 2D simulation, which maximized impact from radiant heat transfer in a microchannel. Much larger reductions in size are expected when comparing with current heat exchanger designs for $scCO_2$ that are not optimized for radiant heat transfer.

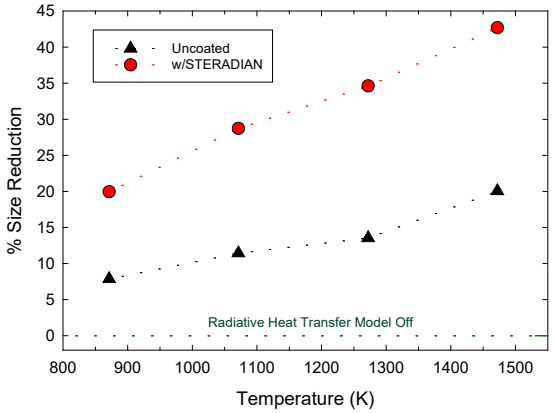

Figure 38. Heat exchanger size reduction versus heat source temperature for a HX with an 80% effective SEC and one without

6.0 Conclusion

In this project, designs for selective thermal emission coatings were generated that shift a significant fraction of the broadband optical emissions from a hot surface into a narrow band in the mid-IR where it is absorbed directly by a $scCO_2$ working fluid. Computational fluid dynamics simulations show that the same approach temperature for $scCO_2$ can be obtained with a much smaller size of heat exchanger due to the enhanced radiative heat transfer produced via implementation of the SEC on the heat exchanger surfaces.

Two different structural motifs for the SEC were considered during the project: thin films and photonic crystals (PhCs). Thin film designs included distributed Bragg reflector, coupled mode, and epsilon-near-zero refractory 1D metamaterials. PhCs considered included cavity, pillar, and cross-bar style designs. The thin-film SECs were found to have high emittance over the target wavelength range and have potential to be very manufacturable as they are tolerant of variation in layer thicknesses and can be built with mature thin film deposition processes. No delamination was observed in the limited thermal cycling that was done under this project but more work is required to demonstrate sufficient thermal stability in a $scCO_2$ heat exchanger application. Several DBR samples were produced and their emissivity properties measured. Reasonable agreement between predicted and measured emissivity was found in some samples but not in others. Root causes of these discrepancies may be in compositional or morphological differences between the thin-film design and as-fabricated samples.

Predicted emissivity profiles for the cross-bar PhC designs developed on this project were shown to offer very narrowband performance and a high overall figure of merit in terms of radiated power in the mid-IR. PhCs also have potential for superior thermal ruggedness due to fewer interfaces with differing materials and contrasting thermal expansion coefficients. Our PhC designs also incorporated a capping layer that enables protection of underlying metals that might be susceptible to reactions with trace amounts of O_2 or H_2O present in the hot $scCO_2$ working fluid. The drawback of PhCs is the requirement for sophisticated lithography to create the periodic sub-wavelength structures. There are some promising scaleable manufacturing techniques that could be applied to produce PhCs, which could be investigated on a follow-on project. Fabrication of the cross-bar PhC design was attempted via stepper and e-beam lithographic methods. Unfortunately, post-process etching to remove mask layers severely degraded the fidelity of the cross-bar features relative to the design and impaired the selective emission properties. Improvements to the etching protocols will be required to generate PhC structures that better meet design specifications.

7.0 References

1. Iverson, B.D., T.M. Conboy, J.J. Pasch and A.M. Kruizenga (2013) Supercritical CO_2 Brayton Cycles for Solar-Thermal Energy. *Appl. Energy* **111**, 957-970.
2. Ortega, J., S. Khivsara, J. Christian, C. Ho, J. Yellowhair and P. Dutta (2016) Coupled Modeling of a Directly Heated Tubular Solar Receiver for Supercritical Carbon Dioxide Brayton Cycle: Optical and Thermal-Fluid Evaluation. *Appl. Therm. Eng.* **109**, 970-978.
3. AlZahrani, A.A. and I. Dincer (2018) Energy and Exergy Analyses of a Parabolic Trough Solar Power Plant Using Carbon Dioxide Power Cycle. *Energ. Convers. Manage.* **158**, 476-488.
4. Zhang, X.R. and H. Yamaguchi (2011) An Experimental Investigation on Characteristics of Supercritical CO2-Based Solar Rankine System. *International Journal of Energy Research* **35** (13), 1168-1178.
5. Zhang, X.R. and H. Yamaguchi (2008) An Experimental Study on Evacuated Tube Solar Collector Using Supercritical CO_2. *Appl. Therm. Eng.* **28** (10), 1225-1233.
6. Jiang, Y., E. Liese, S.E. Zitney and D. Bhattacharyya (2018) Design and Dynamic Modeling of Printed Circuit Heat Exchangers for Supercritical Carbon Dioxide Brayton Power Cycles. *Applied Energy* **231**, 1019-1032.
7. Caliot, C. and G. Flamant (2014) Pressurized Carbon Dioxide as Heat Transfer Fluid: In Uence of Radiation on Turbulent Flow Characteristics in Pipe. *AIMS Energy* **2** (2), 172-182.
8. Khivsara, S.D., V. Srinivasan and P. Dutta (2016) Radiative Heating of Supercritical Carbon Dioxide Flowing through Tubes. *Appl. Therm. Eng.* **109**, 871-877.
9. Streyer, W., K. Feng, Y. Zhong, A.J. Hoffman and D. Wasserman (2015) Selective Absorbers and Thermal Emitters for Far-Infrared Wavelengths. *Appl. Phys. Lett.* **107** (8), 081105.
10. Tsai, M.W., T.H. Chuang, C.Y. Meng, Y.T. Chang and S.C. Lee (2006) High Performance Midinfrared Narrow-Band Plasmonic Thermal Emitter. *Appl. Phys. Lett.* **89** (17).
11. McGrail, B.P., J.J. Jenks and B.E. Bernacki (2020) *Heating Assemblies, Heat Exchange Assemblies, Methods for Providing and/or Exchanging Heat, Turbine Combustion Engines, and Methods for Powering Turbine Combustion Engines*. United States Patent & Trademark Office, Patent No. 17/062,259, USA.
12. Ilic, O., P. Bermel, G. Chen, J.D. Joannopoulos, I. Celanovic and M. Soljacic (2016) Tailoring High-Temperature Radiation and the Resurrection of the Incandescent Source. *Nature Nanotechnology* **11** (4), 320-324.
13. Celanovic, I., N. Jovanovic and J. Kassakian (2008) Two-Dimensional Tungsten Photonic Crystals as Selective Thermal Emitters. *Appl. Phys. Lett.* **92** (19), 193101.
14. Yang, Z.-Y., S. Ishii, T. Yokoyama, T.D. Dao, M.-G. Sun, P.S. Pankin et al. (2017) Narrowband Wavelength Selective Thermal Emitters by Confined Tamm Plasmon Polaritons. *ACS Photonics* **4** (9), 2212-2219.
15. Yang, Z.-Y., S. Ishii, A.T. Doan, S.L. Shinde, T.D. Dao, Y.-P. Lo et al. (2020) Narrow-Band Thermal Emitter with Titanium Nitride Thin Film Demonstrating High Temperature Stability. *Advanced Optical Materials* **n/a** (n/a), 1900982.

16. Dyachenko, P.N., S. Molesky, A.Y. Petrov, M. Störmer, T. Krekeler, S. Lang et al. (2016) Controlling Thermal Emission with Refractory Epsilon-near-Zero Metamaterials Via Topological Transitions. *Nat. Commun.* **7** (1), 11809.

17. Yeng, Y.X., M. Ghebrebrhan, P. Bermel, W.R. Chan, J.D. Joannopoulos, M. Soljačić et al. (2012) Enabling High-Temperature Nanophotonics for Energy Applications. *Proceedings of the National Academy of Sciences* **109** (7), 2280-2285.

18. Heinzel, A., V. Boerner, A. Gombert, B. Bläsi, V. Wittwer and J. Luther (2000) Radiation Filters and Emitters for the Nir Based on Periodically Structured Metal Surfaces. *Journal of Modern Optics* **47** (13), 2399-2419.

19. Li, Z.G., L. Stan, D.A. Czaplewski, X.D. Yang and J. Gao (2018) Wavelength-Selective Mid-Infrared Metamaterial Absorbers with Multiple Tungsten Cross Resonators. *Opt. Express* **26** (5), 5616-5631.

20. Caliot, C. and G. Flamant (2014) Pressurized Carbon Dioxide as Heat Transfer Fluid: Influence of Radiation on Turbulent Flow Characteristics in Pipe. *AIMS Energy* **1** (2), 172-182.

Pacific Northwest National Laboratory

902 Battelle Boulevard
P.O. Box 999
Richland, WA 99354
1-888-375-PNNL (7665)

www.pnnl.gov